Quantum Enhanced Accelerometer using NV Centres in Diamond

Roel Mouris

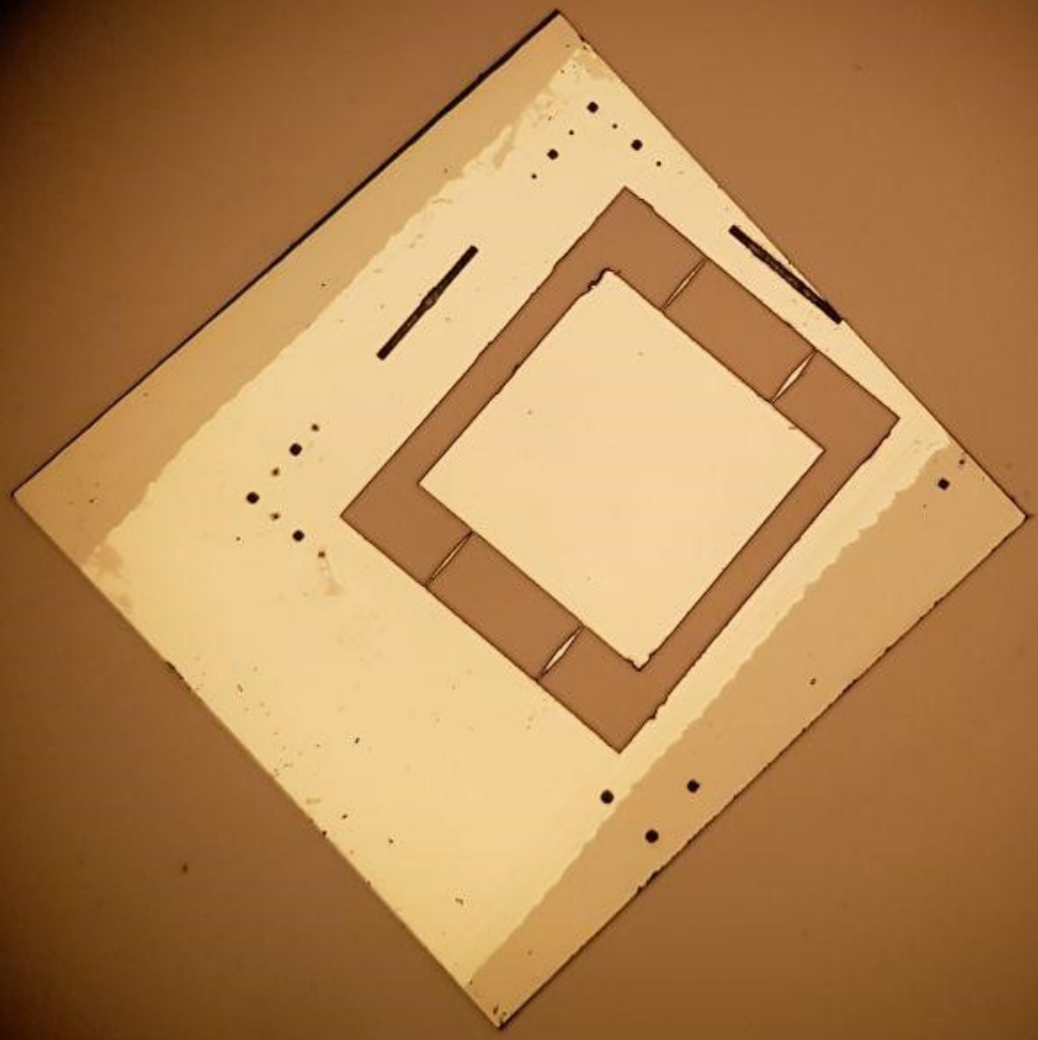

TU Delft

Quantum Enhanced Accelerometer using NV Centres in Diamond

by

Roel Mouris

to obtain the degree of Master of Science
at the Delft University of Technology,
to be defended publicly on Monday December 19, 2019 at 10:00.

Student number:	4243404	
Project duration:	June, 2018 – December 19, 2019	
Thesis committee:	Dr. R. Ishihara,	TU Delft, supervisor
	Prof. dr. P.J. French,	TU Delft
	Prof. dr. P.M. Sarro,	TU Delft

TU Delft

Abstract

Silicon accelerometers used in the automotive industry should be improved in resolution and accuracy. Exploiting quantum effects in diamond to improve sensing accuracy is a popular technique for nanoscale sensing applications. This thesis will present a new design concept for an accelerometer using these quantum effects for sensing on a macroscopic scale. This sensor can sense these forces with a resolution of 6g and a range of 120g. In measurement time it is slower than current sensors, but our sensor can still serve as a prototype to be improved in the future.

Acknowledgements

I would like to thank all people that helped me during my work on this project. Special thanks go to:

- Oscar for supervising me, even after his contract ended.
- Paolo for helping me with nickel etching in the EKL MEMS lab furnace and tuning the recipes.
- Kavli staff for being helpfull in solving fabrication issues.
- Johannes for helping me measure my samples optically in EKL.
- Brecht for teaching me how to use the annealer and cleaning recipes.
- Koos for implanting my samples.
- Emilie for helping me with measurements in Hasselt and Milos for letting me use the equipment.
- Ryoichi for the project.
- Lina and Paddy for being in my thesis committee.

Roel Mouris
Delft, December 2019

Contents

1 Introduction

In this chapter, a brief introduction to airbag systems is given along with the motivation to why it is important to enhance their performance and the areas in which they can still be improved. The main objective of this work is also discussed and serves as an introduction to the following chapters.

Nowadays more and more sensors are being built into cars. The main reason for this is that these sensors are getting cheaper every year. Their reliability and accuracy are also continuously improving. Most of these sensors are Micro Electro Mechanical Systems (MEMS). MEMS are usually made of silicon and use tiny structures to electrically read out the quantity to be measured. One of these devices is an accelerometer which is used to measure the force of an impact. This determines if an airbag has to inflate. The amount of inflation and the time to inflate the airbag is determined based on the sensor output. When a car hits a wall at 30 km/h the passengers will get a softer airbag than when a car hits a wall at 80 km/h [1]. The amount of deceleration is therewith higher so that the body will use the full space between the seat and steering wheel to always reduce the injury rate as much as possible. Overall these airbags, and with that the sensors that determine to inflate them, do a great job in saving lives [2]. There are however also reports of injury due to a wrong inflation of an airbag [3]. This means there is still room for improvement in accuracy of the sensors.

The first vehicle with an airbag system was launched in 1973 [4]. The sensor used for this system was a ball-in-tube sensor as shown in figure 3.1a. It consists of a ball in a tube that is pulled to one side with a magnet. If the deceleration force is higher than the magnetic force, the ball will move to the other side of the tube where a sensor detects it. This sensor is therefore a threshold sensor. In the nineties the MEMS sensor arrived[5], shown in figure 3.1b. This is a more sophisticated sensor. It also consist of a big mass, but this time suspended by springs. The deceleration is measured by a change in capacitance between the mass and the bulk silicon. The main advantage is that it can measure a range of forces, so that the airbag system can adjust to that. This report will describe the next generation of sensors using quantum phenomena in diamond. It also uses a mass to transfer the deceleration force into movement, this movement results in a strain, which is read out using colour centres. This type of sensor could eventually lead to a bigger range and higher resolution than current day sensors. The aim of this thesis is to show that it is possible to exploit quantum effects in NV centers in diamond to build an enhanced accelerometer.

The following chapter describes the background information for this thesis. It contains basic information regarding the airbag system along with more detailed information on diamond and colour centres. Chapter three contains information on previous work, showing the current state-of-the-art accelerometers. This chapter also describes fabrication processes and selected sensing applications. The fourth chapter, called Design and Simulation, describes the design process. This chapter also includes a section regarding simulation of the accelerometer using COMSOL Multiphysics and MATLAB. Chapter five describes the fabrication process of the proposed accelerometer in this work. The measurements of this device are described in chapter six, and the final conclusions are given in chapter 7. The last chapter of this work is chapter 8, it covers the furure work that could be done in order to improve our proposed sensor.

2
Background information

This section will give a short introduction to the airbag system and a more elaborate look on the physics behind the sensor. It will explain the properties of diamond and will discuss what colour centres are and how to use them.

2.1. The airbag system

The airbag system is a system that consists of multiple sensors, actuators and control elements. The first step in this system is to always know at which place the passengers are via pressure sensors in the seats. The second step is to notice a collision, therefore multiple accelerometers sent their values to the control unit. This unit decides if there is a collision or just a bump in the road and with that information decides if the airbags should deploy. This is step three, modern cars can control the amount of gas in an airbag and the speed at which it deploys[6]. This makes the system adjustable to the severity of the impact. Accurate sensors are therefore important, the more advanced the deployment gets, the more advanced the sensors need to be.

2.2. Diamond

Diamond is well known as a hard material. It consist of carbon atoms in a lattice structure that is the same as silicon. Every carbon atom has 4 connections to neighbouring atoms as can be seen in figure 2.1. Orientation is an important factor for the material properties, there are two main orientations: $\langle 100 \rangle$ and $\langle 111 \rangle$. The $\langle 100 \rangle$ orientation is easier to grow and therefore a bit cheaper. The nitrogen-vacancy (NV) centre can have 4 different orientations in this type of diamond. The $\langle 111 \rangle$ oriented diamonds are harder and grown NV centres have over 90% chance to be in 1 preferred orientation[7], more information on NV centres is in chapter 2.3.

This structure is what makes diamond so hard, there is almost no room for the individual atoms to move. However, the number of lattice defects changes the rigidity of the structure. Most occurring natural diamonds have planar defects, because during the natural diamond forming process, the carbon atoms transform into diamond at various locations. When they grow to each other the chance of them lining up perfectly is off course very small and therefore the bonds between these two crystals contain defects. These types of diamonds are called multi crystalline diamonds. Smaller defects such as vacancies, which are empty spaces in the lattice, or impurities, these are different atoms that take the place of carbon atoms, play a smaller role in the hardness and strength of a diamond sample. Natural diamonds in the $\langle 100 \rangle$ direction have a hardness of 56-102GPa.[8]

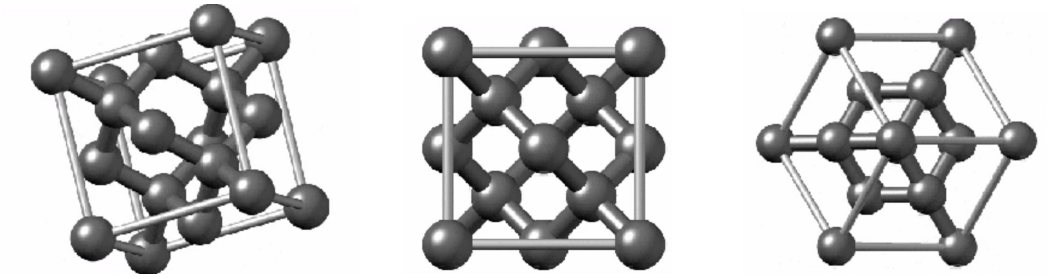

(a) Diamond structure (b) (100) plane (c) (111) plane

Figure 2.1: The diamond lattice and its orientations.

The diamonds used in this project are chemical vapour deposition (CVD) grown single crystal diamonds. These have a low concentration defects, both planar and smaller ones. Therefore the hardness is higher, around 137GPa when the diamond is in the $\langle 100 \rangle$ direction and even 167 when a $\langle 111 \rangle$ diamond is used. [9]

The tensile strength of diamond is more important than the hardness of diamond, there is very little research done on this topic. Simulations show that the weakest plane in terms of tensile strength is the (111) plane, with a strength of 95GPa for a perfect crystal lattice.[10] The strength in the other crystal planes is so high that force in whichever direction will always cleave in the (111) plane.[11]

Natural diamonds can be found in a lot of different colours, the most common are blue, when there are boron atoms in the diamond lattice, yellow, with nitrogen atoms in the lattice, and brown, which means there are defects in the lattice. Diamonds without impurities and defects are clear, they have no colour. The amount of colour is an indication for the amount of impurities or defects in the diamond lattice. For sensors the diamonds should be as clear as possible with only single impurities at the places of readout. These single impurities are called colour centres.

2.3. Colour centres

Colour centres are point defects that make a material appear to have a different colour. A material that can host these effects is diamond. Pure diamond has no colour, it is clear as glass. Impurities give it colours, nitrogen for a yellow colour and boron for blue are common ones, but there are a lot more colours that exist. If the impurities are only one atom or standard group of atoms, it is called a colour centre. The colour centre used for this project is the nitrogen-vacancy centre. It consists of a nitrogen atom that replaced a carbon atom in the diamond lattice and an empty position next to it. In the diamond crystal structure, every carbon atom has a binding to four other carbon atoms. The empty position can be at one of the four positions next to the nitrogen atom, the nitrogen vacancy (NV) centre therefore has four possible directions. The vacancy consists of 5 electrons, 3 from dangling carbon bonds and 2 from the nitrogen atom. A system with 5 electrons will result in a doublet state and the NV centre has a triplet state[12]. Calculations show that the system must consist of 2 or 6 electrons. [13] It is however also proved that the NV centre is negatively charged[14, 15]. This leads to the conclusion that the NV centre system is comprised of 6 electrons, 3 from dangling carbon bonds, 2 from the nitrogen atom and 1 trapped electron.

These single NV centres in diamond are interesting for quantum applications because of their energy structure. Most of the research is focused on quantum networks [16] and nanoscale sensing applications [17]. These colour centres namely operate in the quantum regime and therefore react to tiny disturbances in their surroundings. Operating in the quantum regime means that the energy level structure of an NV centre is quantized, there is a clear distinction between two energy levels that cannot be occupied. Another important thing is that it is possible to control the spin state the system is in, because it depends on the energy levels.

A representation of the energy level system of an NV centre can be seen in figure 2.2. Shown are the ground state $^3\mathrm{A}_2$ and excited state $^3\mathrm{E}$ with three spin levels and states $^1\mathrm{A}_1$ and $^1\mathrm{E}$ which consist of only 1 level. Shining on an NV centre with a green 532nm laser excites electrons from the ground state to the excited state. The energy difference between these two levels is 1.945eV. A 532nm photon has an energy of 2.32eV, but since radiative transition is spin preserving the electrons in the $^3\mathrm{A}_2\,|0\rangle$ state can only go to the $^3\mathrm{E}\,|0\rangle$ state and the same holds for the ± 1 states. The electrons will fall back, but the route they take depends on the spin state. Electrons in the $^3\mathrm{E}\,|0\rangle$ state have a high probability of falling down to the $^3\mathrm{A}_2\,|0\rangle$ state, which emits a photon with a wavelength of 637nm. The $^3\mathrm{E}\,|\pm 1\rangle$ states however have a high probability going back via the singlet levels and are therefore dark, because a photon with wavelength 1046nm is infrared and thus not visible for the human eye. [18]

It is also possible to let the electron state cycle between the $\mathrm{m_s} = 0$ level and the $\mathrm{m_s} = \pm 1$ levels. In the $^3\mathrm{A}_2$ state the energy needed for transition is 12μeV, using $E = hf$, this gives a frequency of 2.87 GHz. In the $^3\mathrm{E}$ state, this energy is 5.9μeV corresponding to 1.42GHz.[19] Matching a microwave frequency to these values changes the quantum state of the electron. The population in each level follows an oscillating motion. The frequency at which this happens is called the rabi frequency and the motion rabi oscillation.

Another way to manipulate the energy level diagram is by splitting the degenerate $\mathrm{m_s} = -1$ and $\mathrm{m_s} = +1$ levels. This can be done in various ways. The most common one is using a magnetic field, but

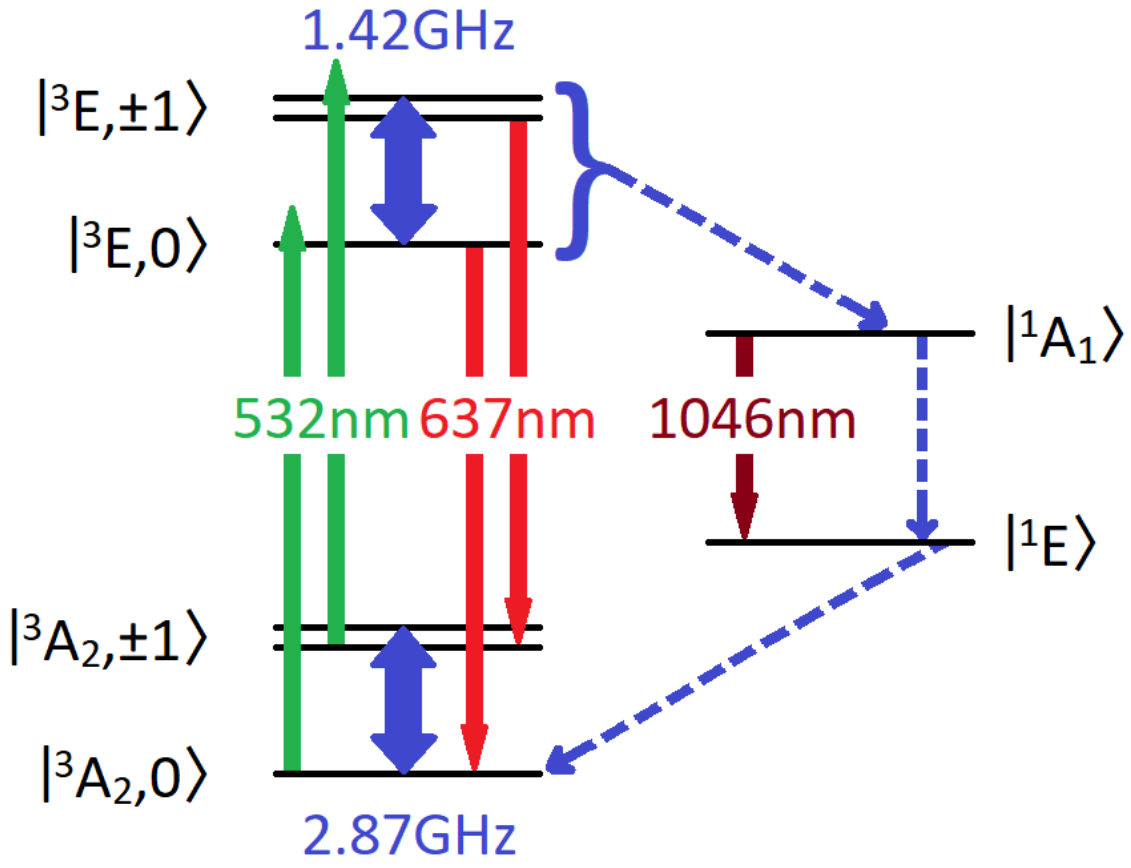

Figure 2.2: Energy level diagram of an NV centre

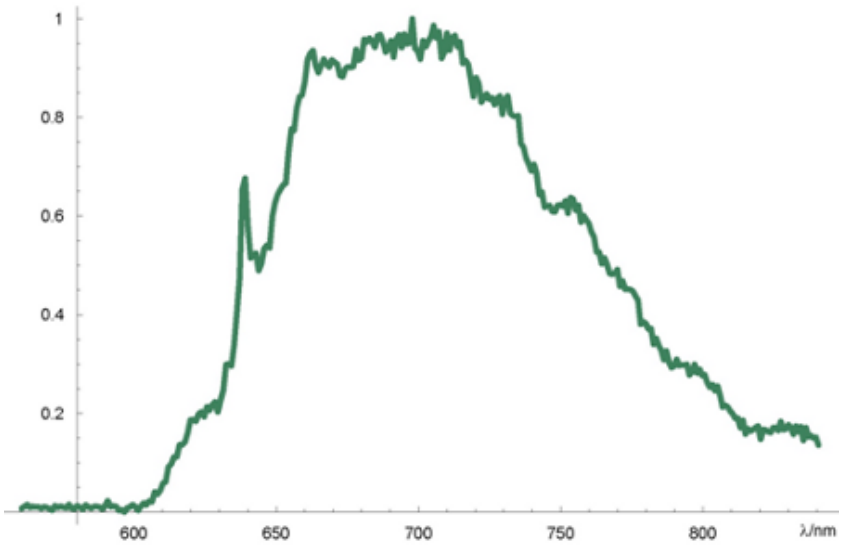

Figure 2.3: Fluorescence spectrum of an NV centre. Taken from [22]

it is also possible to use an electric field[20] or an elastic field[21]. When a magnetic field is used, this effect is called the Zeeman effect, in case an electric field, the term Stark effect is used and the elastic field effect is not named yet. The outcome is however the same for all these effects, the $\mathrm{m_s} = -1$ level decreases in energy and the $\mathrm{m_s} = +1$ increases. This is only the case if the fields are aligned parallel with the NV centre main axis. That happens when the field is in line with the lattice axis between the nitrogen and the vacancy that together make up the NV centre.

Figure 2.2 shows that the emitted light from the NV centre should be 637nm, this is however not entirely true. The spectrum of one NV centre is given in figure 2.3. It shows that a broad spectrum of light is emitted. The first peak in the graph correspond to the zero phonon line (ZPL). A phonon is the energy of a vibration in the lattice structure of a material, diamond in this case. Light that is emitted at the ZPL is therefore at the lowest energy state possible, this line is at 637nm. The light that is emitted in the phononic sideband has extra energy due to phonons and that causes the NV centre to have a broad spectrum.

This thesis aims to read out strain in diamond that is an effect of a force. To do this, the coupling between strain and NV centre energy levels is needed. This coupling is described by the Hamiltonian. The Hamiltonian is a description of the total energy of a system, in this case an NV centre. It is established by measuring the effect of certain perturbations on the NV centre. This leads to multiple Hamiltonian's being developed. Some only using the terms perpendicular to the NV centre axis[23], others using all six terms of a strain matrix[21]. Perpendicular strain splits the $\mathrm{m_s} = -1$ and $\mathrm{m_s} = +1$ energy level, where parallel strain shifts both levels equally.[24] Both are interesting for this project, so this thesis will use the Hamiltonian containing all six terms of the strain matrix. This Hamiltonian is given in equations 2.1-2.8. Where H_m represents the magnetic field effects on the Hamiltonian, with *D* = 2.87GHz is the zero-field splitting, ***S***=(S_x, S_y, S_z) is the vector of Pauli matrices, γ_e = 2.8MHz/G is the electron gyromagnetic ratio and **B** is the magnetic field. The ϵ values are the elements of the strain matrix, the h stands for Planck's constant and the h_{ij} parameters couple strain to energy. The values for these parameters are given in table 2.1.

Parameter	value (MHz/strain)
h_{43}	2300
h_{41}	-6420
h_{25}	-2600
h_{26}	-2830
h_{15}	5700
h_{16}	19660

Table 2.1: Table with parameter values to use in the Hamiltonian [21].

$$H = H_m + H_s \tag{2.1}$$
$$H_m/h = DS_z^2 + \gamma_e \mathbf{B} \cdot \mathbf{S} \tag{2.2}$$
$$H_s/h = H_{s0} + H_{s1} + H_{s2} \tag{2.3}$$
$$H_{s0} = [h_{41}(\epsilon_{xx} + \epsilon_{yy}) + h_{43}\epsilon_{zz}]S_z^2 \tag{2.4}$$
$$H_{s1} = \frac{1}{2}[h_{26}\epsilon_{zx} + h_{25}(\epsilon_{xx} - \epsilon_{yy})]\{S_x, S_y\} \tag{2.5}$$
$$+ \frac{1}{2}(h_{26}\epsilon_{yz} + h_{25}\epsilon_{xy})\{S_y, S_z\} \tag{2.6}$$
$$H_{s2} = \frac{1}{2}[h_{16}\epsilon_{zx} + h_{15}(\epsilon_{xx} - \epsilon_{yy})](S_y^2 - S_x^2) \tag{2.7}$$
$$+ \frac{1}{2}(h_{16}\epsilon_{yz} + h_{15}\epsilon_{xy})\{S_x, S_y\} \tag{2.8}$$

In this chapter a brief introduction to the way airbag systems work was given. It also described the physical structure of diamond and colour centres within it, and more specifically, the energy level configuration for the NV centre was explained and how it can be influenced and manipulated by external fields.

3
Previous work

There is off course some work to build upon. Researchers have made structures in diamond, read out strain in diamond using NV centres and there are already very good accelerometers built using silicon. This chapter will discuss them.

3.1. MEMS sensors

Currently, most accelerometers used for airbag systems use silicon MEMS sensors. They are divided into two classes: central sensors and satellite sensors. Central sensors sit close to the airbag electronic control unit. This system is positioned in the middle of the car and is used as the main sensor. Satellite sensors are positioned around the car to deliver additional information about the outer body parts, since there are crumble zones, these body parts experience an acceleration that is different from the central sensor during impact. The airbag electronic control unit uses input from all sensors to determine the kind of crash and the safety measures it needs to take. This report will focus on the central sensor, because it is easier to fabricate, since these are single-axis or at most dual-axis sensors. Sensing more axis like satellite sensors do would require a more complicated fabrication process that is too big for a master thesis project.

The central sensor is usually a single-axis sensor that can be oriented such that it measures primarily in x or y direction. Forces at a frontal collision are between 35*g* and 100*g*, while side impacts can cause forces of up to 250*g*. Where *g* stands for gravitational force equivalent; 1*g* is equal to $9.8\mathrm{m/s^2}$. With a focus on frontal impact sensors, table 3.1 can be made. This table shows that most frontal collision sensors use a range of roughly 120*g*. An error of 5% is also common. Other specifications vary, the NXP sensor is faster but has a lower resolution.[25] The read out delay is the time it takes for a sensor to give a result after impact, it is thus a measure of the total time it takes the sensor to sense the impact force. The goal in this report is to design a proof of concept accelerometer using NV centres to be at least comparable to current day sensors. This means a range of 120*g*, a resolution of at least 9 bits, an error of 5% and a read out delay of maximum 1ms.

3.2. Diamond fabrication

Fabricating diamond is difficult, because of its material properties. The main property causing problems is the hardness. This hardness makes it very difficult to etch diamond, although it can be etched with oxygen and some other gasses in a plasma, finding a mask that degrades less is a hard task. A paper by Dzung Tran[28] has investigated a couple of metals that can be used as a hard mask, they found that aluminium with a ratio of 56 gives the best selectivity. This means that the mask should be relatively

Manufacturer	Range (*g*)	Resolution (bits)	Sensitivity error (%) room temperature (full range)	Read out delay (µs)
NXP [25]	125	9	5 (7)	117
STMicroelectronics [26]	120	13	5 (7.5)	filter dependent: 976, 507 or 273
Bosch [27]	128	12	5 (unknown)	”the first milliseconds of a crash”

Table 3.1: Table showing accelerometers used as central airbag sensor.

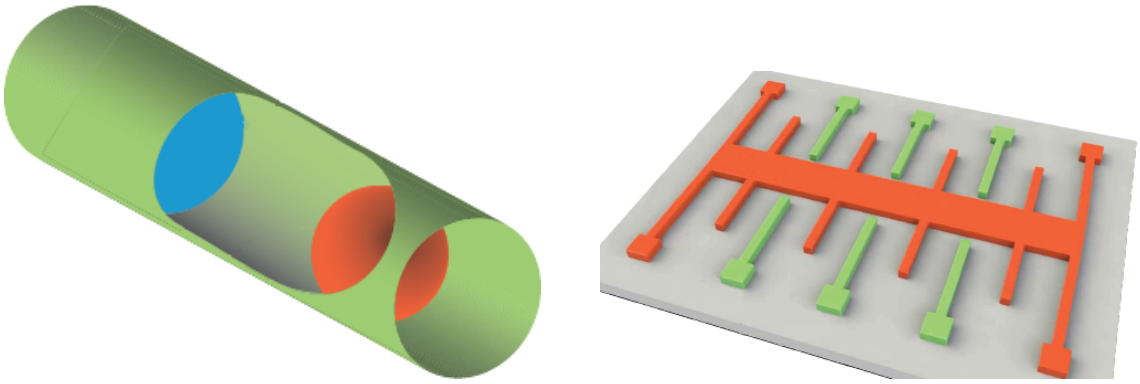

(a) Ball in tube sensor (b) MEMS accelerometer

Figure 3.1: Schematic of two acceleration sensors.

thick. There are also papers discussing a technique that is less common in standard silicon processing. This technique requires a metal layer, mostly nickel, but sometimes iron is used, on top of diamond that works as a catalyst for removing the carbon underneath.[29–32] With this layer on top, the diamond is put in a high temperature (800-1000°C) hydrogen atmosphere. These hydrogen atoms react with carbon atoms that diffuse into the catalyst to form methane. This technique is an-isotropic, it etches (100) planes faster than (111) planes. Other fabrication techniques are better suitable for structures in the nanometer scale, this include focused ion beam milling and transferable mask lithography.[33]

The creation of NV centres is also important. There are two ways to do this. The first is in the growth process, mixing nitrogen with carbon during the growth process will lead to NV centres[34]. The other way is to implant nitrogen by impinging nitrogen ions on a target[35]. These papers also show that grown NV centres are superior to implanted ones. Although there are ways to improve the properties of implanted NV centres, such as post-irradiation and annealing.[36] The main benefit of implantation is that the placement can be controlled by masking the diamond or by focused implantation[37].

3.3. Strain sensing

Sensors using the NV centre are mainly used for nanoscale or quantum sensing applications.[17, 38] Strain sensing applications are not yet reported, although some groups have characterised the influence of strain on the energy levels of an NV centre. Static strain is researched by analysing strain behaviour in an anvil.[39] This shows that the energy change in state splitting has a linear correspondence with pressure and therefore strain. Other groups tried to use induced dynamic strain to gain better control over the spin state by using cantilevers containing an NV center[40, 41] or using an acoustic resonator attached to the diamond[42]. These papers show that it is possible to cause spin transitions using only strain. These are magnetically forbidden and are therefore promising for control of the spin state in an NV centre.

3.4. Approach and method

All accelerometers consist of three main parts: A mass to convert acceleration into displacement, springs to control the position of the mass, and a measuring part to read out the displacement of the mass. First accelerometer designs used a ball as the mass, a tube with a slope as the spring and a touch sensor as the measurement device. A schematic of this design can be seen in figure 3.1a. A big change happened with the introduction of MEMS sensors shown in figure 3.1b. The entire device is made of silicon, however all the main distinctive elements can still be found. The mass consists of a big block of silicon, the springing action is performed by a small beam and the way to measure has become capacitive. The purpose of this thesis is to show what the mass, spring and readout of a quantum enhanced accelerometer would look like. However, before we can design the accelerometer, ther are a few questions that need to be answered: how should the mass spring and readout system be connected?, what should the size be?, how big will the readout signal be within this design?. The second step will be to fabricate this design, which also raises questions: what kind of process to use?, how do we protect the diamond substrate?, what parameters to use for nitrogen implantation?. The

last step will be to measure the device and produce a final answer to all of these questions.

This chapter described the technology currently being used in commercial accelerometers, the latest fabrication techniques used for diamond and the state-of-the-art on strain effects measurements and applications in colour centres in diamond.

4

Design and Simulation

The purpose of this chapter is to describe what the mass, spring and readout system of a quantum enhanced accelerometer would look like. This will be done on the basis of simulations performed in COMSOL Multiphysics and MATLAB. Finally, the last part of this chapter will give an estimation of the read out signal that can be expected from this device.

4.1. Dynamic strain

To start designing, the requirements in the previous chapter have to be transformed to work for a quantum enhanced accelerometer. A paper by Macquarrie[42] describes a way to control the spin transitions in an NV centre using strain induced by an acoustic resonator. It shows that a high frequency in the order of GHz is needed for usable readout. So ideally the resonance frequency should be in this order, therefore the size of the structure should be very small. This makes the first design to have a low weight and high stiffness to make this high frequency possible, this however impacts the amount of strain. When the stiffness goes up, the displacement will be less and therefore the strain will be less. The low weight also reduces the strain resulting from impact.

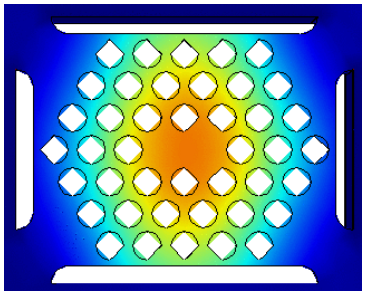

Figure 4.1: Top view of a design of a diamond slab containing a photonic crystal that meets the frequency requirements. The slab is suspended by four springs in the corners. These are very short and relatively wide, which gives them their high stiffness. The size of the slab (1.5x1.2µm) and its thickness (0.5µm) together with the holes for the photonic crystal make it very low in weight.

Because of this low strain, the readout should be improved to get a reasonable light response from the nitrogen-vacancy (NV) centres. A possible solution that improves the light response is the use of a photonic crystal to confine the photons inside the area around the NV centre so that more of the captured light is in the zero phonon line instead of the phonon side band. According to Shao, Liu and Zhou[43]: ”Photonic crystals (PCs) are highly ordered materials that possess a periodically modulated dielectric constant, with the properties of confining and controlling the propagation of light owing to the existence of photonic band gap, a band of frequencies in which light propagation in the photonic crystal is forbidden”, ”which facilitates control of the spontaneous emission and propagation of light.” The photonic crystal proposed for this project consists of a lattice of holes. The minimum size for it to work is 1.2µm by 1.5µm, but a larger size will have a better effect. This minimum size photonic crystal is too big to put on the originally designed suspended slab, so the slab is made bigger to precisely fit the photonic crystal. This however creates some new problems. First of all the strain is highest in the springs and not in the centre of the slab. To try to counteract this, different shapes are made to try to make the slabs strain maximal in the centre. This can be done by making the slab antisymmetrical. Another problem that arises using the photonic crystal is that the holes significantly reduce the weight

of the slab and therefore reduce the strain created on impact. These problems are hard to overcome, so there needs to be a complete redesign with a different readout scheme.

4.2. Static strain

Beginning all over, the first aim is to look at the effect of strain on an NV centre. According to the paper of Udvarhelyi [21] strain splits the +1 and -1 level just like a magnetic field does. This splitting can be read out using an optically detected magnetic resonance (ODMR) measurement (see chapter 6.3). This can be done within a microsecond, with the aim to readout the reaction to a force within a millisecond, the structure can be mode to move slow in comparison to the readout. To get inspired, modern day MEMS sensors are a good source to look at. The capacitive readout of the structures of these MEMS sensors is made with fins sticking out of the mass and out of the bulk material. If the area between these two changes, the capacitance changes. These fins are placed along the mass to even out errors and any minor shape changes of the mass under a strain force. This design is therefore used as starting point for the redesign of the quantum enhanced sensor.

Taking a design like the one showed in figure 3.1b, a few things have to be changed. Putting the measurement at roughly the same spot means that the fins have to undergo a strain. Strain is already present in the springs of this system. It is therefore a good idea to combine the springs and readout into one. Because diamond is a very hard material, the springs will be very stiff. In order for the mass to move and create a reasonable amount of strain in the springs, it is decided to use only 4 springs. Using also the photonic crystal, the first design is shown in figure 4.2a.

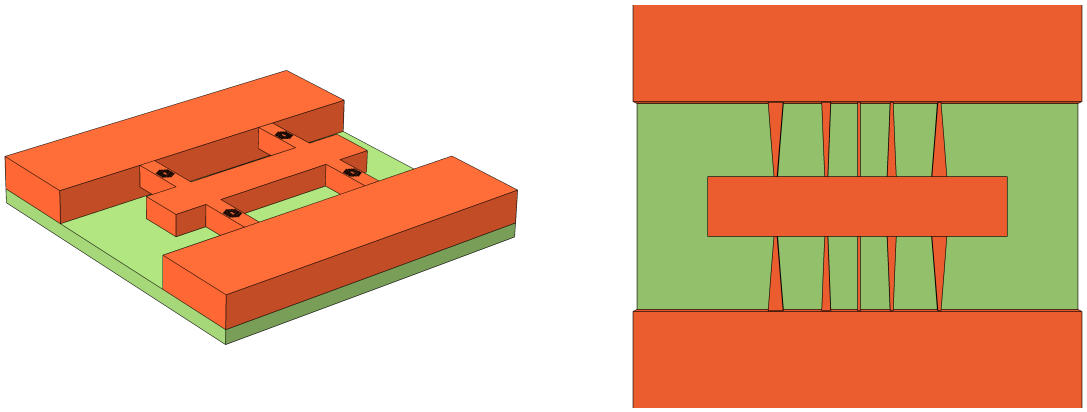

(a) New design with a photonic crystal

(b) Design to see the behaviour of different shaped beams

Figure 4.2: Two design iterations

Simulating this design brought forward some new problems. The photonic crystal mechanically weakens the diamond and therefore the strain is less. The next design will not feature a photonic crystal because of this. A second problem is that the strain is still not high enough. There are several ways to make it higher, first of all, the springs are made thinner, so that they are more flexible. This makes the mass move further and therefore the strain will be higher. The second way is to focus the strain into one point. Strain is dependent on the amount of bending that is inside the spring. To focus the strain, the spring should keep straight as much as possible and bend only at one point. This can be done by shaping the beams, at the thinnest point is the most strain. It is easier if the readout points stay at the same spot during an impact, so the thinnest point is made at the point the spring attaches to the bulk. The NV centres should thus also be implanted at these points. Reducing bending in the rest of the spring is done by shaping it. A triangular shape is made, because it is one of the most rigid shapes[44]. This design does not the high strain that was expected, but it is unclear why. That is why a test structure is build using triangles that point from the mass to the bulk and the others that point from the bulk to the mass. Another differentiation is made in using different widths. The structure can be seen in figure 4.2b. This structure gives some insight in what went wrong. The strain is focused well in the thinnest point, but the structure does not move, because it is too stiff. This stiffness is a consequence of the inability for the springs to hinge. The springs should thus be able to hinge at both sides, but not bend in the middle, because then the strain is not focused anymore.

4.3. Final design

This brings us to the final design. Putting two triangles together to create rhombus shaped springs. To create a linear device, at least two springs per side are needed. In total that makes 4 springs. The width of this springs is dependent on the amount of strain needed for readout. How much is needed depends on the measurement equipment and readout time. The aim is to measure the impact force within one millisecond. A measurement setup is not yet build at the time of design, but since the end goal is to integrate everything on chip, a low to medium quality is estimated. The strain should be maximised to get a high resolution, but the device should not break during high acceleration. In section 2.2 the maximum stress a perfect crystal lattice diamond can handle is given to be 95GPa. To be on the safe side, we chose to aim for a maximum stress of 5GPa at 120*g* acceleration. This results in a strain of roughly 0.005 and with that a sensitivity of $4e^{-5}$ per 1*g* acceleration. The adjustments that can be made to the springs are their width in the middle and their length. The width of the endpoints is fixed to 1µm, because of reliability issues when it is made smaller and less movement of the mass if it is made bigger. Also fixed is the depth of the springs, in the early designs it had the same depth as the mass for ease of fabrication. Since this makes the springs too stiff, they are now set to 50µm. This value ensures the springs are less stiff, but still makes sure there is no up/down movement due to perpendicular forces. It can be made smaller, but controlling the height is very difficult in manufacturing, so having this height also eases the constraints in fabrication.

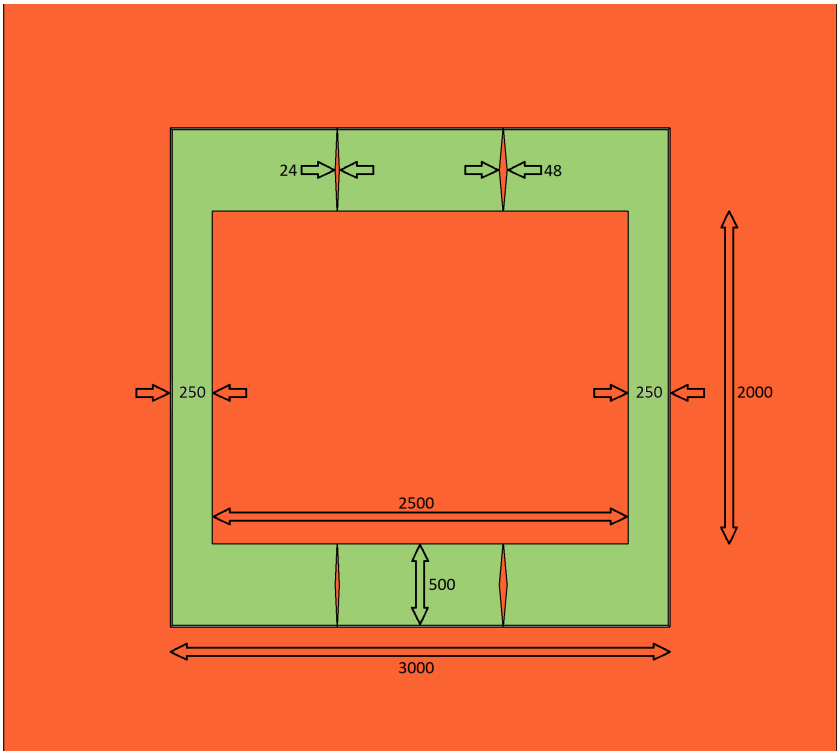

Figure 4.3: The final design with its sizes in µm.

Getting back to the design of the springs with the fixed sizes above, the only change can be made in shape and length. The length is a more influential parameter on the whole system, so it is easier to get the right value for this first. To be able to bond the diamond to a wafer, 1mm of space is left on all sides of the diamond. The available diamond is 5x5mm, this leaves an area of 3x3mm to make the structure. The length of the mass should be maximal to get to the highest mass possible. A higher mass creates a higher force, which in turn creates a higher strain. There should be some room to move for this mass, so it is not possible to make it 3mm. A gap of 250µm at both sides should be enough, so the total length is set to 2.5mm. To get high strain, the springs should be small and the mass should be as big as possible, but should also be able to move. Using COMSOL Multiphysics to simulate different lengths for the springs, a good compromise is found in making the springs 500µm long. This gives the springs enough possibility to hinge and it means the mass itself will be 2mm wide, which gives it a high

enough mass to act on the springs. An overview of this design can be seen in figure 4.3.

The last thing to decide on is the width of the springs in the middle. Making all the springs the same size would give them all the same level of strain, so making one wider than the other would give a higher strain in the wider spring. It is not a good idea to make the difference too big, because this will make the device more sensitive to off axis acceleration. The chosen ratio is therefore 1:2, one of the beams is twice as wide as the other. To define the exact width, the mechanical resonance frequency is calculated. Looking at table 3.1, force readout within $1\mathrm{ms}$ is a decent value, this means maximum deflection should be within $0.9\mathrm{ms}$, because a little time is needed to process and sent the signal to the main control unit. Using equation 4.1, a minimum resonance frequency of 556Hz is calculated. Using COMSOL Multiphysics a frequency of 564Hz is eventually achieved with a width of 24µm for the small spring and a width of 48µm for the big spring.

$$frequency = \frac{1}{time[s]} = \frac{1}{2 * 0.0009} = 556Hz \tag{4.1}$$

4.4. NV centre response

Having this design, the next step is to see what kind of readout values are expected. The structure is simulated in COMSOL Multiphysics, but this cannot simulate the effect on NV centres. To calculate the reaction of an NV centre to strain, the Hamiltonian is needed. This is the equation that describes the behaviour of a colour centre to its environment, such as a magnetic field, electric field and also a strain-induced field. The coupling parameters and equation for the Hamiltonian are given in a paper by Udvarhelyi [21].

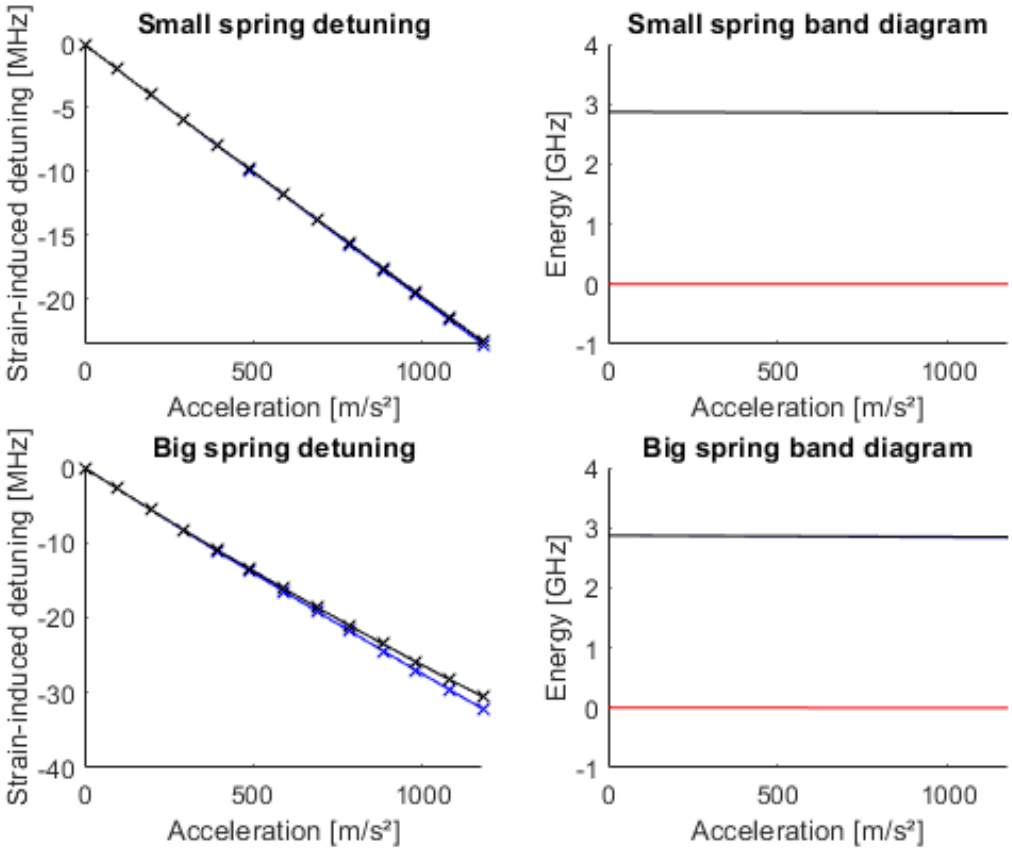

Figure 4.4: Band diagrams and detuning of the simulated device. In the graphs for detuning, the blue line corresponds to the change in the difference between the $\mathrm{m_s} = 0$ and the $\mathrm{m_s} = -1$ sub-level. The black line displays the change in difference between the $\mathrm{m_s} = 0$ and the $\mathrm{M_s} = +1$ sub-level. In the band diagrams, the red line is the $\mathrm{m_s} = 0$ sub-level and the black line are the $\mathrm{m_s} = \pm 1$ sub-levels. Since they are on top of each other, it is not possible to differentiate them.

The resulting Hamiltonian gives some extra insight in what the readout would look like. An energy level diagram is shown in figure 4.4. Since the amount of change in energy with regard to the applied strain between the $\mathrm{m_s} = 0$ and the $\mathrm{m_s} = -1$ sub-level is small compared to the total energy difference between those levels, it will be a good idea to bring them closer together. Adding an axial DC magnetic field will do this, while the shift due to the strain stays the same. This means that the relative shift will be much higher and therefore that the readout equipment can be less sensitive.

There is however a catch with this, if the levels are too close together, they will experience a phenomenon called avoided crossing. When it seems like the energy levels would cross each other, they exchange energy. This leads to them repelling each other and therefore they will never cross. An example is shown in figure 4.5. This phenomenon makes the difference between the $\mathrm{m_s} = 0$ and the $\mathrm{m_s} = -1$ sub-level non-linear, so it is better to stay away from the avoided crossing point.

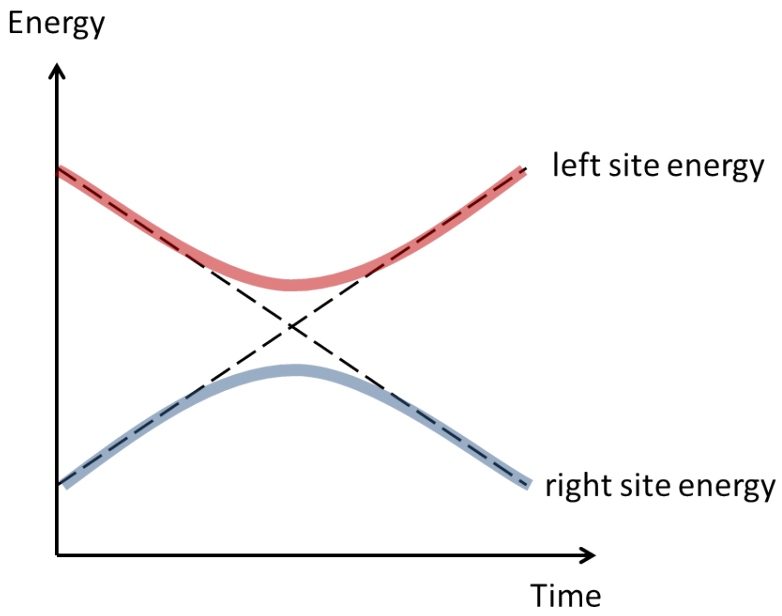

Figure 4.5: A schematic of an avoided crossing.[45]

This means there is an optimum magnetic field to bring the two levels as close as possible but without degrading the linearity of the detuning too much. To find the correct value for the magnetic field, the first thing to do is to get the energy of the sub-levels, then the difference between the $\mathrm{m_s} = 0$ and the $\mathrm{m_s} = -1$ sub-level can be calculated. The linearity can be checked by finding the deviation from a straight line between detuning at an acceleration of $0\mathrm{m/s^2}$ and $1177\mathrm{m/s^2}$. The greatest deviation is normally halfway this line, so we calculated the deviation at $588\mathrm{m/s^2}$. Doing this for multiple values of the magnetic field B, results in the graph in figure 4.6. A linear response is desired, because the sensitivity and resolution will be constant over the whole range. To keep the linearity within 3 percent, the graph tells that a good value for B is 858 Gauss. But only if the small spring is used, the big spring is already out of specification with a B field that is a lot smaller. These springs are however still needed in the design to get the right mechanical resonance frequency.

Applying a magnetic field lowers the $\mathrm{m_s}$=-1 sub-level a lot closer to the $\mathrm{m_s}$=0 sub-level. This means that the relative change under strain will be a lot larger. The energy difference between these levels goes to 468MHz instead of 2.87GHz, while the absolute change stays the same. This means that the relative change improves by over 6 times. The final energy band diagram is shown in figure 4.7.

This chapter described the process by which an accelerometer is designed. Simulations were a big part of this process, since they provide a way to understand the behaviour of the device and what parameters to optimise in the design. The end result is a device consisting of a relatively big mass and tiny rhombus-shaped springs with NV centres at the end points. The optimum magnetic field to obtain the biggest effect is also calculated using the NV centre Hamiltonian and is determined to be 858 Gauss.

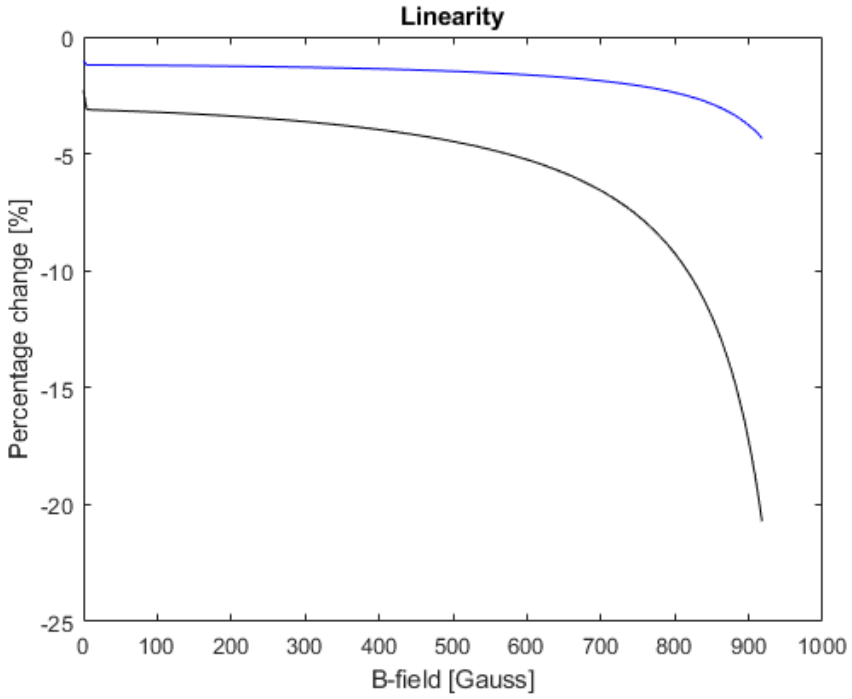

Figure 4.6: Linearity of the difference between the $m_s = 0$ and the $m_s = -1$ sub-level for different magnetic field values. The blue line corresponds to the small spring and the black line is for the big spring. The linearity is given as a percentage. The graph clearly shows there is a drop-off point when the magnetic field gets close to the avoided crossing point.

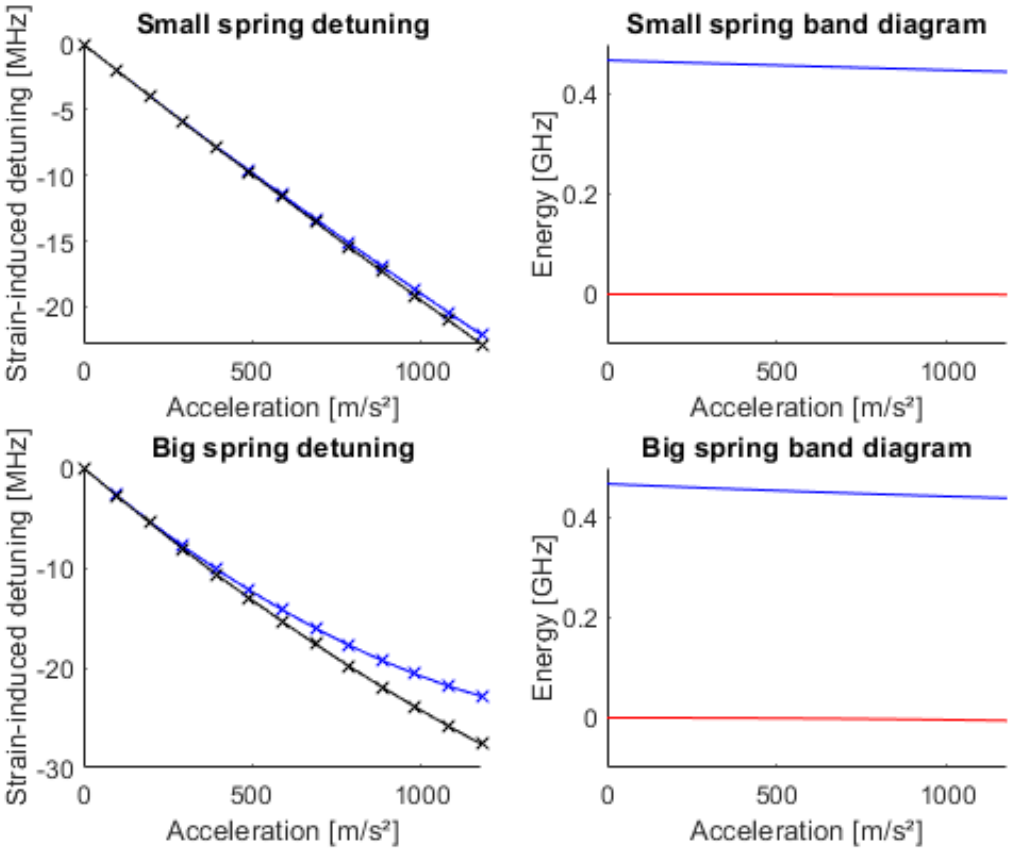

Figure 4.7: Figure 4.7 shows the detuning and energy band diagrams for the simulated device in that is shown in figure 4.3 and with an applied magnetic field of 858 Gauss. In the detuning graphs, the blue line corresponds to the change in the difference between the $m_s = 0$ and the $m_s = -1$ sub-level whereas the black line displays the change in difference between the $m_s = 0$ and the $m_s = +1$ sub-level. In the band diagrams, the red line is the $m_s = 0$ sub-level and the blue line is the $m_s = -1$ sub-level. The $m_s = +1$ sub level is at 5.2 GHz and therefore not plotted.

5 Fabrication

Fabricating the accelerometer requires several steps to be taken, with some of them more prone to failure than others. This chapter will describe the processes that were attempted and at the end will give the full fabrication process that will produce the actual device. The main goal for this device is to create smooth and steep sidewalls. This is done with a trough-diamond etch, this etch does not need to keep a clean surface. There is however also the need for a clean second etch from the bottom to thin down the springs and to make the mass free floating, so that it can still move when it is attached to a measurement substrate.

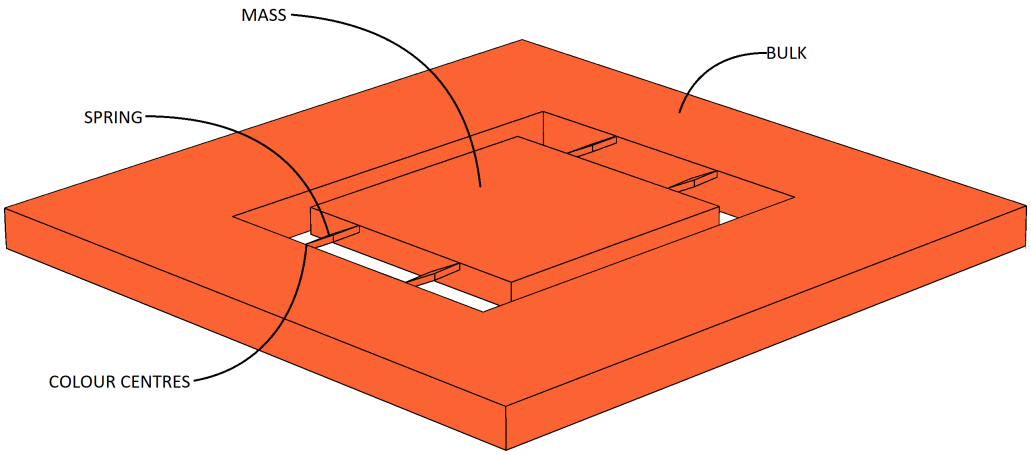

Figure 5.1: 3D structure that has to be fabricated.

5.1. Nickel etching

For the first few designed structures, an an-isotropic etch would be beneficial. A paper by Nagai et al.[29] describes the possibility to etch diamond using nickel in a high temperature water vapour. The theoretical description of the etching process is that a thin layer of nickel is deposited on diamond where the etching is required. This diamond will diffuse into the nickel and then react with water vapour to form gasses that can be pumped out. The uncovered diamond would not react and that means a hole is created under the nickel. This paper reports an etching selectivity of at least 5000 for masked versus unmasked areas. It also states that (111) planes etch a lot slower than (100) planes. The used methods are well described in this paper, so that it could be repeated.

However, when we try this method it shows totally different results: the whole surface roughens and the etching itself is also not as clean as described in the aforementioned paper. Scanning electron microscope (SEM) images taken after etching, but before cleaning of the nickel leftovers are shown in figure 5.2. This clearly shows that the nickel does indeed enhance the etching of diamond, but not in a way that is usable to make clean structures.

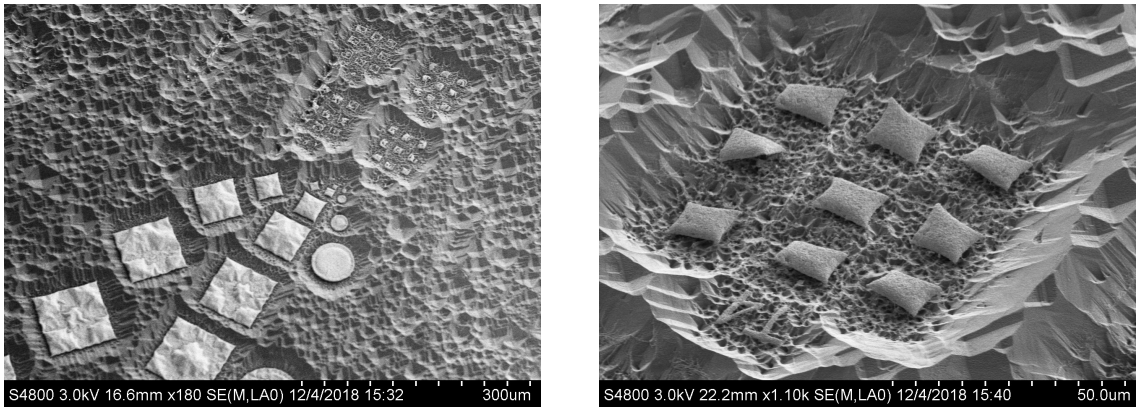

Figure 5.2: SEM images taken after nickel etching, but before removing the nickel. The nickel is clearly distinguishable from the diamond surface. Although the diamond underneath and directly surrounding the nickel did etch, the rest of the diamond surface is also etched and not flat anymore. The pillows in figure (b) where originally small feature size rounds and squares. They have clustered together and formed bigger nickel particles.

5.2. Plasma etching

This means a different etching technique should be used. In chapter 3.2 plasma etching was proposed as a suitable candidate. In the available machine in the Van Leeuwenhoek Laboratory (VLL), the available gasses that can etch diamond are argon chloride (Ar/Cl_2), sulphur hexafluoride (SF_6) and oxygen (O_2). They can be used in combination with each other or standalone. Oxygen is mostly used as etchant, however problems due to micro masking can arise.[46] Micro masking means that the diamond surface contains non-diamond particles that mask the surface giving a change in etch speed. This can lead to the formation of holes or pillars. However, this effect can be mitigated by introducing a second gas that can etch these particles. Research has shown that using first Ar/Cl_2 followed by O_2 is a viable solution if a clean surface is needed. [47]

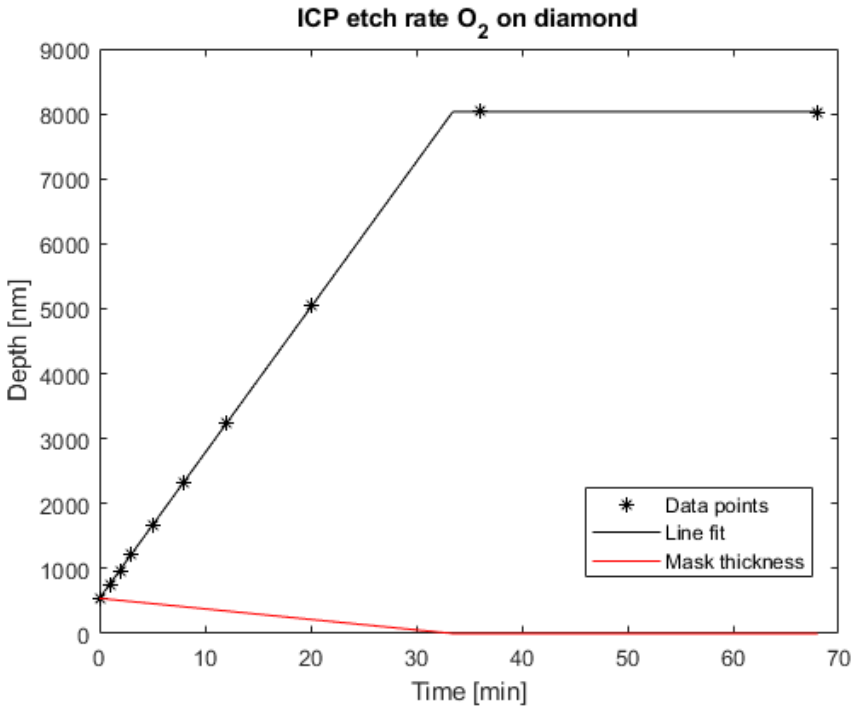

Figure 5.3: Etch rate of diamond using a silicon oxide mask with a thickness of 542nm. After roughly 33.5 minutes the mask is totally removed and a depth of 8033nm is measured. The etch rate of diamond is estimated to be 240nm/min, while the etch rate of SiO_2 is estimated to be 16.2nm/min.

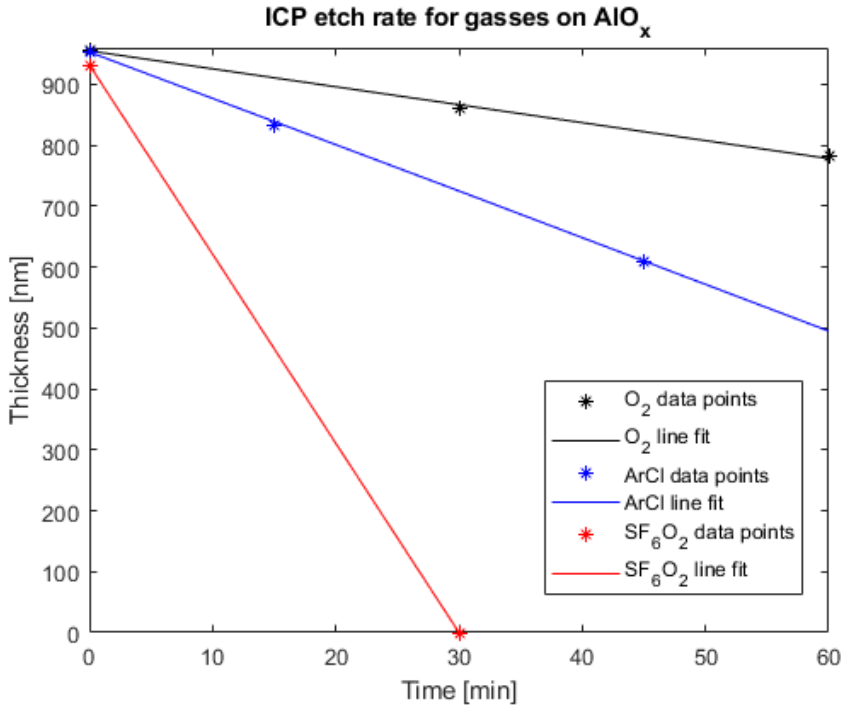

Figure 5.4: Etch rate of aluminium oxide using 3 different recipes. The estimated etch rates are 2.9nm/min for O_2, 7.7nm/min for Ar/Cl_2 and >31nm/min for SF_6.

This last paper mentions a stable etch rate of roughly 40nm/min for Ar/Cl_2, but the etch rate for O_2 varies between 210nm/min for a sample masked with fused quartz and 350nm/min without a mask. The measured etch rate on our diamond samples was about 240nm/min using a 542nm thick plasma-enhanced chemical vapour deposition (PECVD) grown silicon dioxide (SiO_2) mask. This measurement is shown in figure 5.3. A maskless sample was not attempted, because it is not used for our accelerometer structure.

5.3. Masking material

The mask material used for this sample is PECVD grown SiO_2. This mask is consumed at a rate of approximately 16.2nm/min. The selectivity of this recipe is therefore $240/16.2 = 14.8$. To try and improve on this number an aluminium oxide (AlO_x) mask was investigated. Figure 5.4 shows the etching rate results using all three gasses mentioned earlier. The selectivity using O_2 gas on AlO_x is $240/2.9 = 82$. From this results can be inferred that an AlO_x mask has 5.5 times lower etch rates with O_2 etching than SiO_2. This means that the AlO_x mask thickness can be reduced.

For through-diamond etching, a rough surface is not a problem. Because there is no etched surface after etching. Re-deposition of metal can be useful, because it creates passivation of the sidewalls while the energy of the plasma still maintains a clean enough surface to keep etching.[48] Etching only with oxygen is therefore the recipe we use for through-diamond etching.

Next to this etch, there is also the need for a clean surface etch that can thin down the springs and the mass. The diamond samples used for this project are not parallel cut, the height between two corners can vary by as much as 40 micron. This means that etching from the bottom will present extra difficulties with these diamond samples. Which is why the final fabricated structure is different compared to the final design. Processing difficulties leads to the design being only etched from the top, which leads to the mass and springs being the same height. The structure is therefore stiffer than designed.

It proved to be difficult to deposit a layer of aluminium oxide thicker than 2µm in the VLL, while we need at least 4µm. This means that the mask material should be changed. A hard mask made of silicon seems to be an easy solution, because of the availability of wafers and their low cost. The diamonds used in this project have dimensions 5x5mm. In order to not expose the sides too much to the plasma

Figure 5.5: Pictures taken by a SEM show that the non-etched surface of diamond stays clean, whereas the etched surface consists of thousands of nanopillars. The sidewalls are steep, but not smooth.

we choose to use 10x10mm coupons of silicon as mask. The coupons are cut using a wafer dicing machine. These diced coupons are the starting point of the main process as shown in figure 5.6. The standard thickness of a silicon wafer is 500µm, which is too thick to etch through the small structures required. The coupons are therefore thinned down to roughly 200µm using a Bosch process. A 300nm thick aluminium layer is evaporated on top of the coupons to act as a hard mask for pattern transfer. This pattern is written in e-beam resist that is spin coated on top of the aluminium layer. It is transferred into the aluminium using a TMAH wet etch. With a Bosch process the silicon is etched through so that it can be used as mask.

5.4. Etching

This mask is manually aligned to the diamond as good as possible by using previously placed tungsten alignment marks on the diamond and holes in the silicon mask. They are glued together using e-beam resist. After 13.5 hours of oxygen plasma the expected depth of the holes in the diamond is $0.24 * 60 * 13.5 = 194.4$µm. However, the measured depth is 79.2µm and SEM images displayed in figure 5.5 show that micro masking becomes a severe problem when etching this deep, since plenty of pillars appear to have formed.

To improve the etching profile, a 30 seconds etch step of SF6 gas is introduced after every hour of O_2 etching. The diamond used for this etching is not yet implanted, so the alignment is less of an issue. The holes for implantation can be aligned after etching because the alignment markers are also etched into the diamond. The diamond surface also looks slightly rough, this is probably because the backside of the silicon wafer is not polished and therefore not extremely flat. That is why for the next run the silicon coupons were thinned down from the unpolished backside, so that the front stays flat. The aluminium is then evaporated at the front, because the step coverage at the back could be too large for a 300nm aluminium layer to cover. After the structure is etched into the silicon, it is flipped onto the diamond. The aluminium layer is thus in contact with the Polymethyl methacrylate (PMMA) layer that is used to glue the mask to the diamond. All steps are listed in appendix A.

5.5. Implantation

The implantation of nitrogen into diamond is an important part of manufacturing. In an early fabrication attempt the diamond was first implanted and afterwards the structure was partly etched. The alignment of the mask with the diamond was done in a home built setup normally used to transfer graphene layers, see figure 5.7. The alignment was precise up to a few micrometers, but since the springs in the original design are at the ideal point of implantation only 1µm wide, the required accuracy is 500nm. So this alignment is not good enough. Therefore we decided to change the order of etching and implantation. First the diamond is etched by placing the mask on top in roughly the right place. After etching, this mask is removed and the diamond is glued to a clean carrier coupon. This is only needed because the diamond itself is not strong enough to withstand the forces applied when spinning electron-beam resist. The alignment microscope for the electron-beam writer can then be used to assign the right spots of implantation.

The implantation is performed in the Else Kooi Laboratory (EKL). Values for implantation have been obtained using SRIM-2013 simulation software in combination with a paper regarding implantation depths in diamond[49]. The conclusion of this is that the range the simulator predicts is roughly 80% of

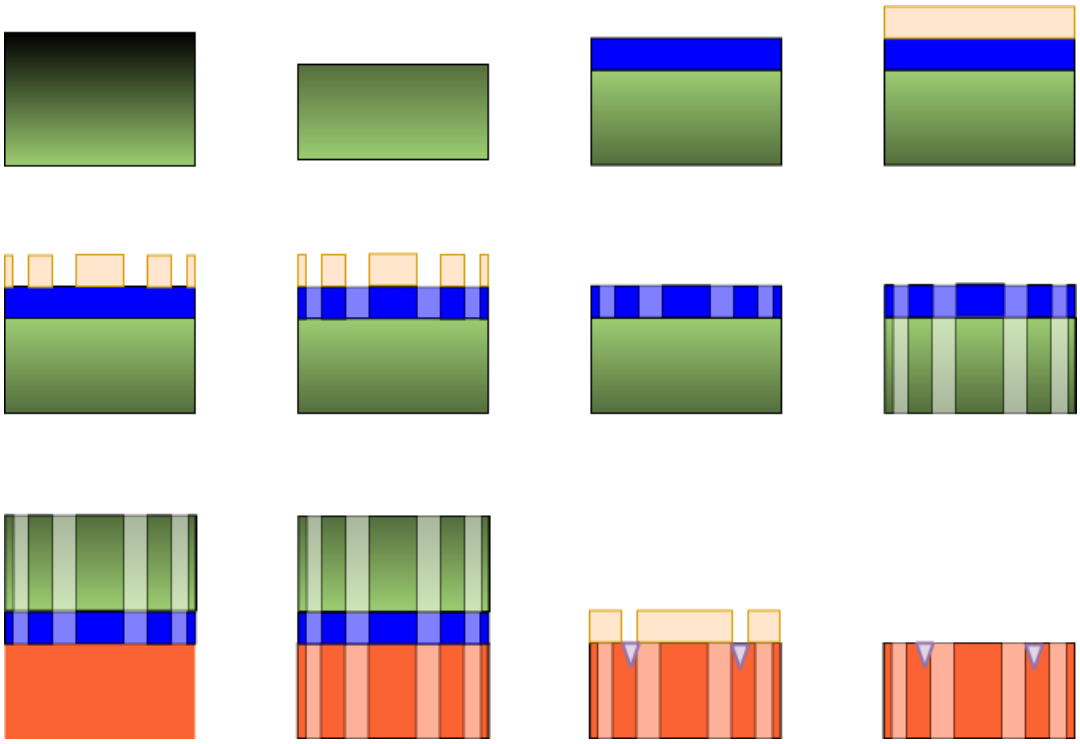

Figure 5.6: Process flow for making the device. We start with fabricating the silicon mask (green). The first step is to dice a wafer into 10x10mm pieces. They are thinned down from the backside (black) to roughly 200µm. A 300nm aluminium layer (blue) is then evaporated on the polished side of the coupon (light green). After this we spin electron-beam resist (pale orange). The next step is to define the device structure and marker holes in the resist. This needs to be transferred to the aluminium. After this the resist is removed and the aluminium mask is transferred into the silicon. This silicon can then be used as a mask to etch the structure into diamond. At this point, a diamond is cleaned and the mask is glued on top using PMMA with the flattest side of the mask touching the diamond. After etching the mask can be removed by dissolving the glue. The next step is to spin a layer of electron-beam resist and pattern the implantation holes. After the implantation, the resist is removed and the diamond is cleaned so that it can finish at the annealing step.

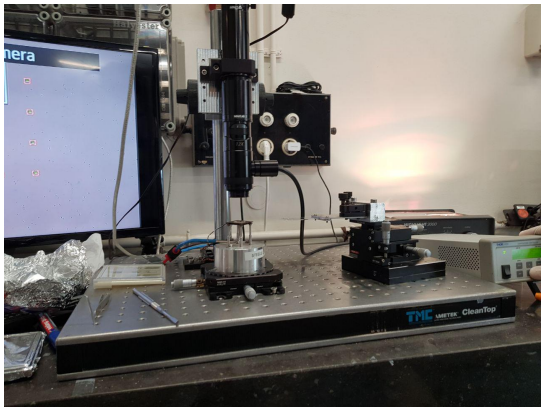
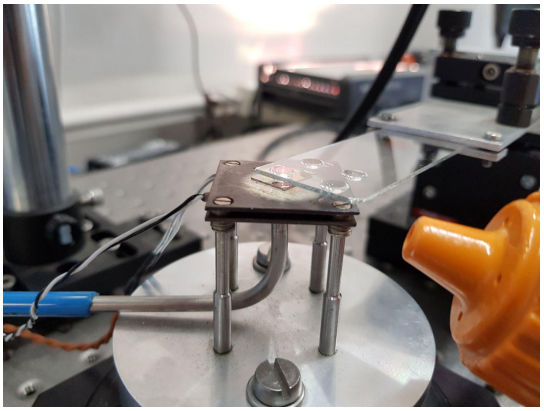

Figure 5.7: The transfer setup, it uses a big microscope with camera to view the area you transfer to, in our case the alignment is done using a white square that the camera can overlay with the image. Using alignment marks on the diamond as well as on the mask.

the actual value. We chose the depth of implantation to be 100nm, because this is deep enough to avoid effects from the diamond surface that change the charge state of the NV centre, which will change its behaviour.[50] Going deeper results in more damage due to implantation and will also increase straggle which leads to inaccuracy in placement. The value in simulation we are therefore aiming at is 80nm, using nitrogen-14 ions, since this is the isotope to be implanted, the simulator showed that the energy should be 36keV. A resist mask with a thickness of 250nm should be able to block these ions from penetrating the diamond, which is convenient, otherwise a different masking material has to be found. This would increase the manufacturing time and number of steps in which something can go wrong. The minimum number of ions that can be implanted by the machine in EKL is $1\mathrm{e}^{11}\mathrm{ions/cm}^2$. We patterned implantation holes with a 100nm diameter, which results in on average 31 ions implanted in each hole as can be seen in equation 5.2.

$$Number \quad of \quad ions = (number \quad of \quad ions \quad per \quad cm^2) \cdot (hole \quad area \quad in \quad cm^2) \tag{5.1}$$

$$Number \quad of \quad ions = 1e^{11} \cdot 3.14 \cdot (1e^{-5})^2 = 31.4 \quad ions \tag{5.2}$$

This chapter described the route to a fabrication process in which the accelerometer is made. Nickel etching was attempted but did not work as expected, so plasma etching was used. The best masking material found was a thinned down silicon coupon fabricated using e-beam lithography and deep RIE. In the end the diamond was implanted and is now ready to be measured. This will be discussed in the next chapter.

6
Measurement

In this chapter, we will have a look at the fabricated device. The goal was to make a device with steep and smooth sidewalls, this will be inspected using visual measurements. Another important part of fabrication was to implant nitrogen ions that will create NV centres. This chapter will therefore cover the detection of NV centres and measurements of their properties.

6.1. Visual inspection

The device fabricated is first visually inspected under a microscope as displayed in figure 6.1. This shows that the topside of the diamond sample has the same pattern and width as the silicon mask, however, the edges appear to be rougher. The backside is slightly worse. Here the springs appear to have a different thickness than the diamond surface, they are less thick than the bulk diamond. During the etching step, we monitor the depth of the opening on diamond sample compared to the carrier wafer on which the sample was glued. To our surprise we found that instead of a hole, there is still a rough plateau several microns high. We therefore can conclude that the etching time was slightly too short.

The device is also inspected under a SEM, resulting in figure 6.2, this shows that the sidewalls are steep, but not smooth and there also looks to be a protecting layer on it. This layer is probably a by-product of the SF_6 gas and thus fluoride enriched. In other processes this would be removed with oxygen at high temperatures, but since this would also affect our diamond, we decided to leave it on. The diamond surface looks as flat as before, which means this was well protected by the silicon mask.

6.2. NV centre detection

Using a simple home-built setup, we measured if there were any NV centres after implantation and annealing. The setup contains a green laser, with a wavelength of 532nm, to excite the NV centres. These NV centres will decay back to the ground state, emitting photons with a wavelength above 600nm wavelength. A filter between our sample and the camera will block the low wavelengths, meaning the light we capture with our camera has a wavelength that is produced by the photo luminescence of the impurities in our diamond sample. We expect to see four bright spots at the spring endpoints. However, figure 6.3a shows that all the edges are bright, suggesting they contain NV centres. The resist should have been thick enough, but it was not taken into account that it tapers off at the edges when a spin coater is used. It should have been spray coated instead.

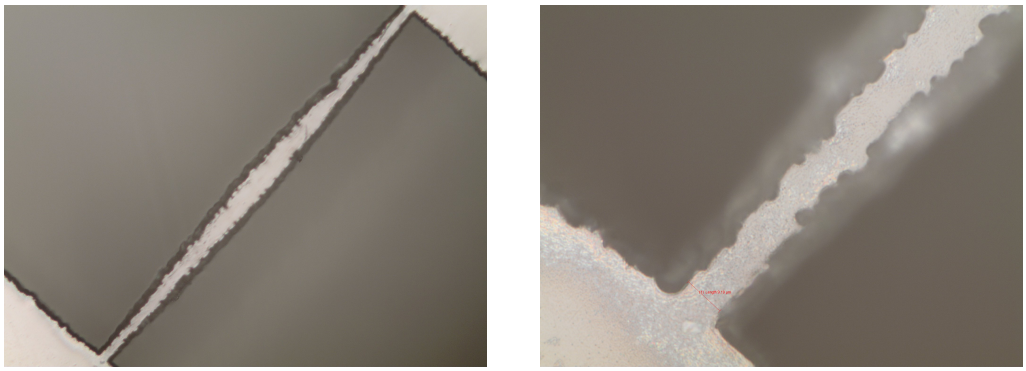

Figure 6.1: Pictures taken by a confocal microscope to show the roughness of the beams.

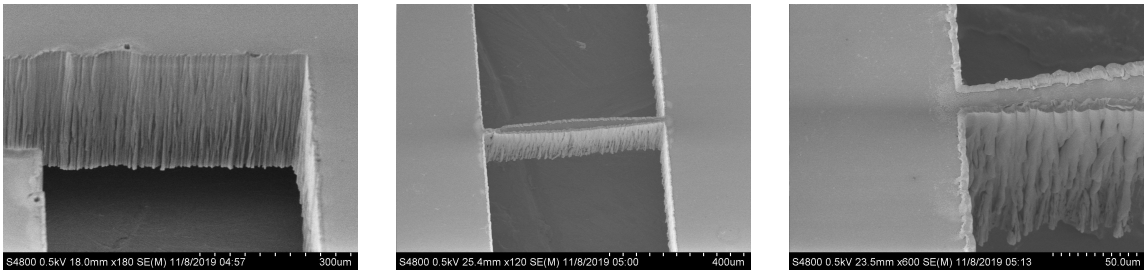

Figure 6.2: Pictures taken with a SEM. They show that the sidewalls are steep, but not smooth and that they are covered with a layer that is most likely fluoride enriched.

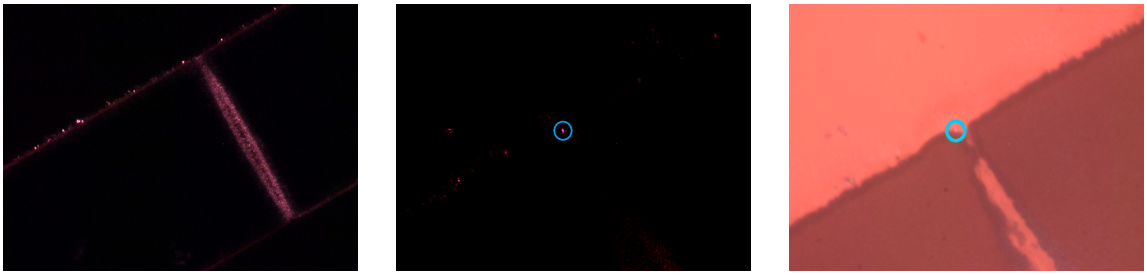

(a) All the edges appear to be very bright

(b) An ensemble of NV centres that could be intentionally implanted.

(c) Same area as figure b with normal light.

Figure 6.3: Pictures taken using the home-built setup. Figure (a) shows one spring and an edge that contain NV centres. These three pictures are taken by a confocal microscope through a filter, figure (a) and (b) with only the green laser turned on and figure (c) with also normal light turned on.

Although there is a lot more illumination than expected, it is still possible to find some bright spots. When we look close at an area where we expected to have implanted, we can see one bright spot that roughly corresponds to its intended position. A green laser and normal light picture of this spot are shown in figure 6.3. The normal light picture is also red, because the filter between the sample and camera was not removed. This picture shows that the bright spot is not in the middle of the spring, where it is intended to be. Instead it is all the way to the edge, which should enhance the response to strain, because the strain at the edges of the spring is slightly higher than in the middle. It is however also possible that being too close to the diamond edge would increase noise due to dangling bonds.

6.3. ODMR

Optically detected magnetic resonance (ODMR) is a measurement method used to detect NV centres and inspect their response to external influences like strain fields, magnetic fields and microwaves (MWs). It works by illuminating the diamond with a green laser with a certain intensity. NV centres in the diamond will photo luminescence at a longer wavelength, just as in the previous measurements. The difference is that this measurements use MWs, sweeping over a range of frequencies will reduce the intensity of light at some of them, depending on the magnetic and strain field. Without any fields there should be one minimum at 2.87GHz as described in section 2.3.

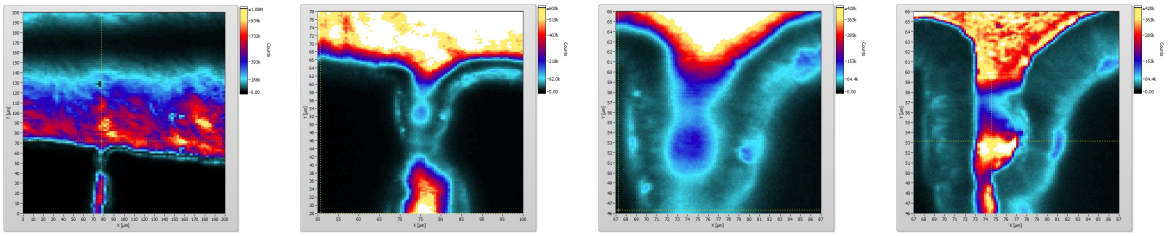

(a) 200x200µm scan.

(b) 50x50µm scan.

(c) Original depth 20x20µm scan.

(d) New depth 20x20µm scan.

Figure 6.4: Light intensity figures of a part of the structure to find the NV centre ensemble that was implanted. Figures (a), (b) and (c) are taken with focus on the surface. Figure (d) is taken with a focus 1.3µm deeper than the others.

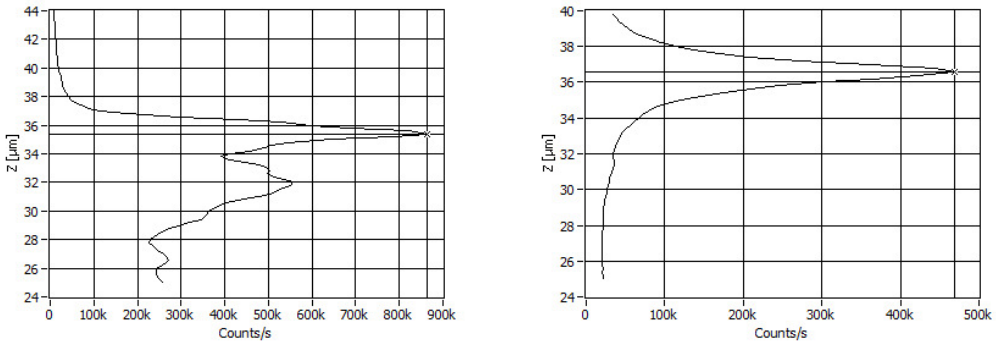

(a) Depth scan at the edge.

(b) Depth scan at the intentionally implanted NV centres.

Figure 6.5: Light intensity versus focus depth. Graph (a) is taken at the point focused at in figure 6.4a, graph (b) is taken at the point focused at in figure 6.4d.

Before we can sweep the MW frequencies we have to find the implanted NV centres. Figure 6.4 shows the process of finding the right spot. First we manually align the diamond to the right spot, then we take a 200x200µm image that shows that the MW antenna, this is the black part in the top of the picture, is close enough to the NV centres in the spring. We then zoomed in on the spot the NV centres should be. Here we found a round spot that is not as bright as the rest of the nearby surface. Since the intentional implanted NV centres should be deeper than the NV centres that are partly blocked by the resist, we did a scan in height, shown in figure 6.5. This shows that the photo luminescence peak for the round spot is deeper than the surrounding area and only peaks at one depth. This should therefore be the intentionally implanted spot. It is however at a different spot than we measured using the home-built setup, the spot measured by that setup is most likely an unintentional surface ensemble of NV centres.

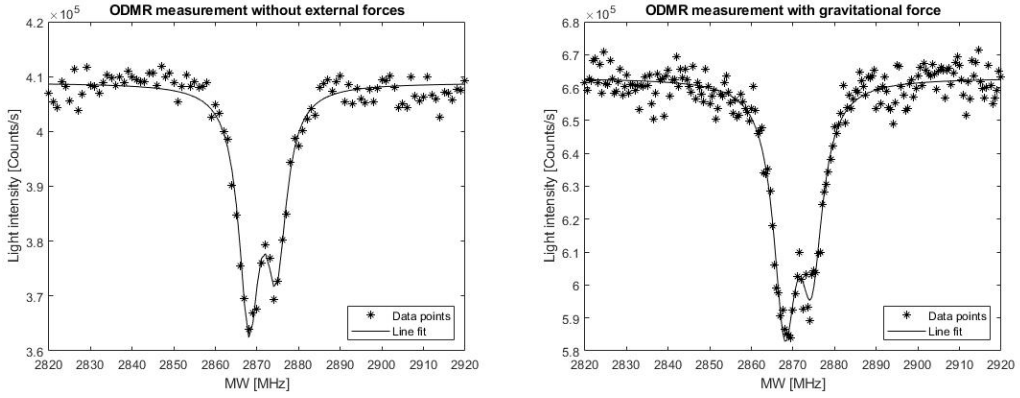

(a) Zero force pulling the mass.

(b) One g force pulling the mass.

Figure 6.6: ODMR measurement without an external magnetic field applied. The difference between figure (a) and (b) is the force pulling the mass. This difference is created by rotating the device, so that the effect of gravity does or does not play a role. The obtained values are averaged over 5 measurements.

An ODMR measurement was done at the intentional implanted spot using 1W MW power and 1mW laser power resulting in a fluorescence graph shown in figure 6.6. Of these two graphs, figure 6.6a shows the light intensity versus the MW frequency where there are no external forces acting on the NV centres. The valley in this graph consists of 8 NV centre resonances that are on top of each other, they can be split using external forces such as a magnetic field or a strain field. The valley has a full width at half maximum (FWHM) of 10MHz. It has a little peak in the middle showing there is a small splitting without external forces, there could be multiple reasons for this. It could be internal strain due to implantation, nearby nuclear spins of carbon-13 or nitrogen atoms or spin-spin interactions between multiple NV centres. The valley is centred at 2871MHz, so that is as expected. The valley in figure 6.6b is also centred at 2871MHz, it has however a FWHM of 11.5MHz. This measurement is taken

after rotating the device 90°, so that gravity is pulling the mass down. This force creates a strain in the beams, which splits the $m_s = +1$ and the $m_s = -1$ levels. Simulations shown in figure 4.7 expect a detuning of 0.25MHz to each side, so 0.5MHz in total, the bigger difference is partly due to the noisy signal, which makes it hard to determine the half maximum value. There could also be mismatch between the measurements and simulations, because the simulations only considered strain in one direction, while there is strain in all directions.

Comparing the light intensity to other samples measured in this setup in Hasselt, we can conclude that the spot we measure contains between 30 and 50 NV centres. In section 5.5 we calculated on average 31 nitrogen ions should be implanted in each hole. Since not all nitrogen ions form NV centres, we can conclude there are, at least in this spot, more ions implanted than expected. The contrast of the measurements in figure 6.6 is 12%.

Adding an external magnetic field results in a splitting of the 8 resonances. Since this reduces the contrast considerably, the MW power was increased to 6W. The resulting ODMR graph is shown in figure 6.7a. It shows 8 clearly distinguishable valleys, an m_s=-1 level and an m_s=+1 level for all 4 of the crystal orientations. Figure 6.7b shows a zoom on the m_s=+1 level resonances, for this measurement we decreased the MW power back to 1W. To obtain a suitable graph we had to average over double the amount of measurements. Despite this, we found that the contrast is decreased from 3% to 2%, while the FWHM is unchanged. The centre of the valleys differ by maximally 1MHz, which is probably due to noise. Lowering the MW power is therefore not necessary for further measurements, they can be done at 6W MW power.

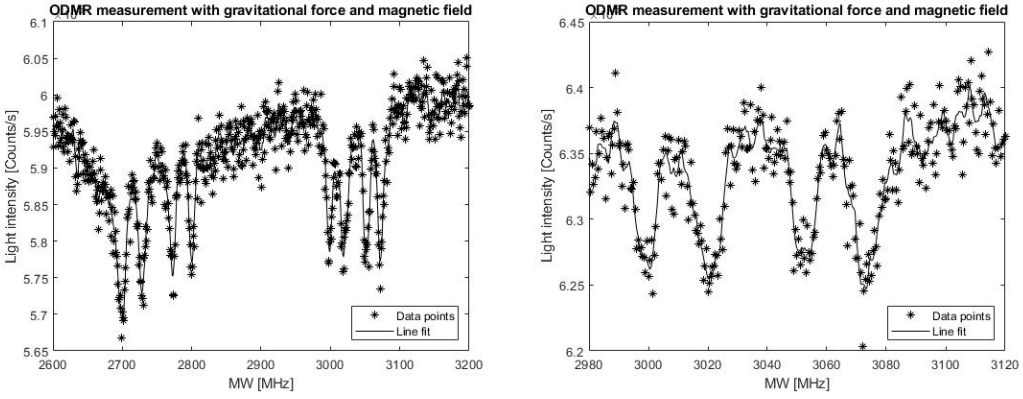

(a) 8 valleys occur due to an externally applied magnetic field.

(b) A zoom on the 4 m_s=+1 valleys using lower MW power.

Figure 6.7: ODMR measurement with an external magnetic field applied. Figure (a) shows all 8 valleys, while figure (b) shows only the 4 valleys corresponding to the m_s=+1 level. For this graph less MW power is used, this decreases contrast, but also creates more narrow valleys. The obtained values are averaged over 10 measurements for figure (a) and 20 measurements for figure (b). The locations for the m_s=+1 level valleys are [3000 3021 3053 3073] with widths [9 10 10 10] and a contrast of 3% for figure (a), and for figure (b) the locations of the valleys are [2999 3020.5 3053 3073.5] with widths [8 10 9 12] and a contrast of 2%.

Adding extra weight to the mass increases the strain in the springs, which increases the splitting of the spin levels. From the difference in splitting between the standard weight and extra weight measurements, the strain field can be calculated in 4 directions. To determine the amount of weight that needs to be added to correspond to the simulations we did, we need to know the weight of the mass we fabricated. The density of diamond is 3515g/(mm^2), resulting in a mass of $M = \rho \cdot V = 3515 \cdot (2.5 \cdot 2.0 \cdot 0.3)e^{-9} = 5mg$. A needle, a small thread and a piece of tape together weigh 160mg, simulating a force of 32 times gravity. In order to stick the combined mass to the diamond, we had to apply a small mechanical force. Unfortunately this was above the limit that our sample could handle and resulted in a broken device. Due to time limitations, it was not possible to fabricate a second device for testing, hence we had to stop the measurements at this point.

This chapter described the measurements that have been done in order to characterise the fabricated device. The sidewalls were steep, but also very rough. NV centres were detected and their properties have been measured, we were able to split the spin levels, but have not been able to measure the influence of strain on them. The next chapter will draw conclusions.

7 Conclusion

This chapter will draw conclusions from the work done. It will discuss if the goals have been met and what has been learned from this project.

It was stated in section 3.1 that: ”The goal in this report is to design a proof of concept accelerometer using NV centres to be at least comparable to current day sensors. This means a range of 120*g*, a resolution of at least 9 bits, an error of 5% and a read out delay of maximum 1ms.”. So, there were 4 main points to be considered: the range, resolution, error and delay. The range has been the main point of focus in the design, since the diamond should not break. In section 2.2 we found that a perfect crystal lattice can handle roughly 100GPa. To be on the safe side we designed our structure to have a maximum stress of 5GPa at 120*g* acceleration. Since the actual range could not be measured, a better way of applying force has to be designed for this.

The resolution of 9 bits has a trade off with the read out delay within 1ms. This delay is the total time it takes for the sensor to output its result from the moment of impact. The simulated structure has a resonance frequency of 564Hz, leading to a maximum strain after 0.9ms, the resonance frequency of the fabricated device is not measured, but should be higher. The second part of the read out delay is the time it takes to do the strain measurement. A measurement in which the MW frequency is swept over a fixed range takes a few seconds. The time to measure one point in our measurements is 50ms. With a read out scheme that only tracks the resonances it should be possible to do readout within 1 second, but this is still too slow to be used as crash sensor. Since we were not able to measure the shift due to extra force with a magnetic field applied it is hard to say what resolution we could get. However, taking into account the amount of noise measured in our experiments, which was roughly 1MHz, we can conclude that the minimum detectable shift should be around 1.5MHz. Simulations in section 4.4 have showed that such a shift corresponds to an acceleration of 6*g*. This is not comparable to current day sensors, but it still can serve as a prototype to be improved in the future.

Noise during read-out is the main cause of errors, it can lead to resonance shifts of around 1MHz corresponding to 4g. There is also a slight non-linearity at high magnetic fields leading to an error of maximum 5%.

Overall, we have presented a new design concept for an accelerometer that tries to improve the resolution of current day technologies exploiting quantum effects. As mentioned before, at this point it is not conclusive whether it could actually outperform current sensors, more research would be needed. Ideas that can lead to improvement will be discussed in the next chapter.

8

Future work

In future designs a lot of improvement can be made. Some of them are not yet implemented design differences, others need different materials or fabrication techniques. This chapter will discuss them.

In order to get undistorted readout, silicon MEMS structures do readout in static state. This can be done in two ways. By applying feedback to keep the mass at the centre or by applying damping so that the excitation is constant. Feedback is not an option for this kind of device, because it depends on the strain inside the diamond, but damping could be integrated. For this, the structure must be enclosed and filled with a gas. The structure can than be designed in a way that the pressure and flow of the gas can give optimal damping characteristics. The main difference with respect to the current design will be in the size of the gaps around the mass. The mass and springs should also be etched from top and bottom to leave a gap to the enclosing package.

Another structural difference that can make an improvement is to differentiate between front and rear impact. Satellite sensors off course also provide this information by having a different timing and outcome, but it would still be beneficial if the main sensor would also provide this ability. This information could also be derived from the shift of all four peaks, since this can be translated to the total strain field. The relation between the shifts and strain field should be characterised using measurements.

With respect to the material usage, there are also improvements to be made. As already stated in chapter 2.2, with the right parameters NV centres grown in $\langle 111 \rangle$ oriented diamond samples have mainly one orientation. Since the influence of strain also depends on the orientation with respect to the NV centre main axis, the design could be adjusted to direct the strain in one orientation instead of just maximising the strain field at one spot. Besides this, the fact that the $\langle 111 \rangle$ orientation has a higher strength as compared to the $\langle 111 \rangle$, could help to extend the durability of the device. A drawback of this would be that no longer a strain field is measured, but only strain in one direction. It would however give a higher signal for this direction.

A more simple improvement can be made in using parallel cut diamonds, so that there is no height variation along the surface. This would ease manufacturing and thus improve the resemblance of the manufactured device with respect to the simulated design.

A key step for making this sensor a success is to integrate the measurement equipment alongside the sensor in a single package. Recently Kim et al. have integrated a MW generator optical filter and photodetector on a single chip. [51] Until 2012 green lasers used neodymium-doped yttrium orthovanadate or other neodymium-doped crystals that create long wavelengths that than had to be converted to green light using nonlinear crystals, cavities and beam splitters. [52] Since 2012 laser diodes exist that do not need this and directly emit green light[53, 54], so it should be possible to also integrate these on a chip.

Alignment of the etching mask should also be improved to get a better aim at the centre of the diamond. Especially when the diamond has to be aligned afterwards to other chips that take care of readout or if implantation has been done first.

Something that is unknown at this point is the quality of the implanted NV centers, since to the best of our knowledge, this is the first sample that has been implanted in order to create NV centers at the EKL cleanroom. It would be good to do more research on this to get a better idea of improvements on this side. The time and temperature of annealing also vary a lot in different papers, so it would be good to research the best recipe for the diamonds in combination with the implantation used for this project. The quality of NV centres and their emission is also important for the measurement time. We measured every point for 50ms, but one point can be measured within 10µs[55]. This would decrease the measurement time enough for the sensor to be used in airbag systems.

Diamonds are very expensive, a way to improve the cost can be to change to other materials. Colour centres have been measured in silicon carbide. [56] Its current use is mainly in power electronics[57]. Using this material would make it easier to manufacture, because of this already existing manufacturing technologies. Especially for mass production this would be a benefit.

This chapter gave some ideas for the continuation of this project. It discussed improvements that can be made to the design and manufacturing process used as well as research that has to be done to create a better understanding of the quality of used processes.

A

Process steps

This appendix will describe the processing steps used to make our enhanced accelerometer. First we have to get the materials that are needed, these are: three silicon wafers and one diamond sample. The as-received diamond will be cleaned in a piranha etch which is a solution that consists of sulphuric acid (H_2SO_4) and hydrogen peroxide (H_2O_2). This cleans only organic materials, since we assume there is no other contamination up to this point. One of the silicon wafers is diced into 10x10mm coupons, which will later be used to produce a mask for diamond etching. The wafers and coupons are cleaned by placing the samples in acetone and into an ultrasound bath for 5 minutes. After a 3 minute rinse with IPA, they can be used for further processing. The two silicon wafers remaining will be placed in a PECVD machine, to do a one hour deposition of SiO_2 at 300°C resulting in a 4µm thick layer. These wafers will be used for handling the coupons and diamond sample. So the preparation steps are:

1. Clean the as-received diamond sample using a piranha etch.
2. Clean the wafers with acetone and ipa (ultrasound 5min acetone+3min ipa)
3. Dice one wafer into 10x10mm coupons
4. Put 2 clean wafers into PECVD for 1 hour SiO_2 deposition at 300°C resulting in 4um of silicon dioxide.

To process the coupons or diamond sample, they first will be glued to a wafer using PMMA. The PMMA is hardened on a hotplate at 180°for 10 minutes. The PMMA can be removed using AR600-71. After removal the sample or coupon should be rinsed with IPA. The steps are:

1. Glue a coupon upside down to a wafer with a silicon oxide layer with PMMA
2. Heat it for 10 minutes at 180°C to harden the PMMA
3. Process
4. Clean PMMA with AR600-71, put it in ultrasound bath for 5 min
5. Rinse with IPA

The etch step is to thin down the coupons from 500µm to 200µm, from the unpolished backside. For this, we use a 50 minute etch using 300sccm SF_6 and 150sccm C_4F_8. A Bosch process alternates those two gasses in a cycle, SF_6 is used for 7 seconds each cycle and C_4F_8 is used 2 seconds each cycle. The power is set to 1800W.

After thinning down the coupons, an aluminium layer is evaporated on the flat top side using an e-beam evaporator. The layer thickness is 300nm.

A pattern has to be written onto the this layer, so that the coupon can be etched. As e-beam resist we use AR-P 6200.09 spun at 3000rpm and baked for 10 minutes at 230°C. This pattern is developed by holding the coupon for 40 seconds in a pentyl acetate bath, after that directly 40 seconds in a bath with a 1:1 mixture of MIBK and IPA, than to a bath of only IPA and at last blown dry using a nitrogen gun. So the steps for patterning are:

1. Spin ebeam resist AR-P 6200.09 at 3000rpm
2. Heat it for 10min at 230°C

3. Write pattern
4. Develop 40 sec pentyl acetate, 40 sec MIBK:IPA, 40 sec IPA
5. Blow dry

Now we have a silicon coupon with an aluminium layer and on top of that a layer of e-beam resist with a pattern. The pattern is transferred into the aluminium layer using a 6 minutes wet etch in MF322 at room temperature.

To transfer the pattern in aluminium to silicon another Bosch etch is used with a slightly different recipe. This time the C_4F_8 gas is used for 2.4 seconds at a flow of 245sccm. The flow and time for SF_6 stay at 300sccm for 7 seconds. The power is also the same with 1800W. To go all the way through the sample this recipe needs to run for 30 minutes.

This coupon can now be used as a mask on the diamond. It is glued to it using PMMA in the same way described above.

The diamond is etched using an inductively coupled plasma (ICP) chloride etcher. The recipe used takes a total of about 38 hours. It also cycles to get rid of sputtered particles on the diamond surface. 1 hour of O_2 is alternated with 30 seconds of SF_6 mixed with O_2 and Helium (He). The O_2 only step uses a flow of 50sccm, 1100W ICP power and 180W RF power at 13mbar pressure. The SF_6 step uses flows of 50sccm SF_6, 5sccm O_2 and 3sccm He. Power is set to 500W for ICP and 2W for RF, pressure is also 13mbar. Both recipes run at room temperature. These recipes cycle 37 times for a total O_2 etch time of 37 hours.

The diamond now has the Right structure, but in able to measure the strain it has to contain NV centres. The implantation holes are defined with the e-beam. Diamond is not conducting, so in order to have high resolution holes a layer of electra92 is spun on top at 4000rpm. This layer is after exposure dissolved in H_2O.

Implantation of nitrogen-14 is done in EKL at 36KeV with $1E^11$ ions/cm^2. Afterwards the diamond samples have to be cleaned before they can enter the anneal oven. Cleaning is done in a mixture of $HClO_4$ with a concentration of 60%, HNO_3 with a concentration of 65%, H_2SO_4 with a concentration of 95% at 120°C for 1 hour.

The recipe used for annealing is to ramp to 400°C in 4 hours, stay there for 4 hours, ramp to 800°C in 4 hours and stay there again for 4 hours. After cooling down, the diamond sensor is ready to be measured.

Bibliography

[1] Fakhri Karray, Otman Basir, Dmitri Axakov, and Viktor Haramina. Variable inflation force airbag inflator, September 28 2004. US Patent 6,796,581.

[2] Donna Glassbrenner. Estimating the lives saved by safety belts and air bags. *Age*, 5:12, 2016.

[3] Stroh E. Molia LM. Airbag injury during low impact collision. *British journal of ophthalmology*, 80(5):487–8, 1996.

[4] Automotive News. *Impalas' 1973 experimental airbags held up.*, 2011. `https://www.autonews.com/article/20111031/CHEVY100/310319928/impalas-1973-experimental-airbags-held-up` [Retrieved April 8, 2019].

[5] Inc. Analog Devices. Sensors for low level signal acquisition. Design Conference 2013, 2013.

[6] Wikipedia. *Airbag*, 2019. `https://en.wikipedia.org/wiki/Airbag` [Retrieved May 13, 2019].

[7] Julia Michl, Tokuyuki Teraji, Sebastian Zaiser, Ingmar Jakobi, Gerald Waldherr, Florian Dolde, Philipp Neumann, Marcus W Doherty, Neil B Manson, Junichi Isoya, et al. Perfect alignment and preferential orientation of nitrogen-vacancy centers during chemical vapor deposition diamond growth on (111) surfaces. *Applied Physics Letters*, 104(10):102407, 2014.

[8] N Savvides and TJ Bell. Hardness and elastic modulus of diamond and diamond-like carbon films. *Thin Solid Films*, 228(1-2):289–292, 1993.

[9] V Blank, M Popov, G Pivovarov, N Lvova, K Gogolinsky, and V Reshetov. Ultrahard and superhard phases of fullerite c60: comparison with diamond on hardness and wear. *Diamond and Related Materials*, 7(2-5):427–431, 1998.

[10] David Roundy and Marvin L Cohen. Ideal strength of diamond, si, and ge. *Physical Review B*, 64(21):212103, 2001.

[11] RH Telling, CJ Pickard, MC Payne, and JE Field. Theoretical strength and cleavage of diamond. *Physical Review Letters*, 84(22):5160, 2000.

[12] N.R.S. Reddy, Neil Manson, and Elmars Krausz. 2-laser spectral hole burning in a color centre in diamond. *Journal of Luminescence*, 38:46–47, 12 1987.

[13] A Lenef and SC Rand. Electronic structure of the n-v center in diamond: Theory. *Physical Review B*, 53(20):13441, 1996.

[14] JP Goss, R Jones, SJ Breuer, PR Briddon, and Sven Öberg. The twelve-line 1.682 ev luminescence center in diamond and the vacancy-silicon complex. *Physical review letters*, 77(14):3041, 1996.

[15] JHN Loubser and JA Van Wyk. Diamond research. *London: Industrial Diamond Information Bureau*, pages 11–15, 1977.

[16] Bas Hensen, Hannes Bernien, Anaïs E Dréau, Andreas Reiserer, Norbert Kalb, Machiel S Blok, Just Ruitenberg, Raymond FL Vermeulen, Raymond N Schouten, Carlos Abellán, et al. Loophole-free bell inequality violation using electron spins separated by 1.3 kilometres. *Nature*, 526(7575):682, 2015.

[17] Romana Schirhagl, Kevin Chang, Michael Loretz, and Christian L Degen. Nitrogen-vacancy centers in diamond: nanoscale sensors for physics and biology. *Annual review of physical chemistry*, 65:83–105, 2014.

[18] LJ Rogers, S Armstrong, MJ Sellars, and NB Manson. Infrared emission of the nv centre in diamond: Zeeman and uniaxial stress studies. *New Journal of Physics*, 10(10):103024, 2008.

[19] GD Fuchs, VV Dobrovitski, R Hanson, A Batra, CD Weis, T Schenkel, and DD Awschalom. Excited-state spectroscopy using single spin manipulation in diamond. *Physical review letters*, 101(11):117601, 2008.

[20] Ph Tamarat, T Gaebel, JR Rabeau, M Khan, AD Greentree, H Wilson, LCL Hollenberg, S Prawer, P Hemmer, F Jelezko, et al. Stark shift control of single optical centers in diamond. *Physical review letters*, 97(8):083002, 2006.

[21] Péter Udvarhelyi, Vladyslav O Shkolnikov, Adam Gali, Guido Burkard, and András Pályi. Spin-strain interaction in nitrogen-vacancy centers in diamond. *Physical Review B*, 98(7):075201, 2018.

[22] LMU University of Munich. *Single Photon Sources*. `https://xqp.physik.uni-muenchen.de/research/single_photon/index.html` [Retrieved August 19, 2019].

[23] Florian Dolde, Helmut Fedder, Marcus W Doherty, Tobias Nöbauer, Florian Rempp, Gopalakrishnan Balasubramanian, Thomas Wolf, Friedemann Reinhard, Lloyd CL Hollenberg, Fedor Jelezko, et al. Electric-field sensing using single diamond spins. *Nature Physics*, 7(6):459, 2011.

[24] Sunuk Choe and Donghun Lee. Strain simulation of diamond nv centers in high q-factor diamond membranes. *Journal of the Korean Physical Society*, 73(1):95–99, 2018.

[25] NXP semiconductors. *MMA26xx, DSI Inertial Sensor*, 1 2017.

[26] STMicroelectronics. *AIS1120SX*, 1 2017.

[27] Bosch. *Passive safety systems*, 2018.

[28] DT Tran, C Fansler, TA Grotjohn, DK Reinhard, and J Asmussen. Investigation of mask selectivities and diamond etching using microwave plasma-assisted etching. *Diamond and Related Materials*, 19(7-9):778–782, 2010.

[29] Masatsugu Nagai, Kazuhiro Nakanishi, Hiraku Takahashi, Hiromitsu Kato, Toshiharu Makino, Satoshi Yamasaki, Tsubasa Matsumoto, Takao Inokuma, and Norio Tokuda. Anisotropic diamond etching through thermochemical reaction between ni and diamond in high-temperature water vapour. *Scientific reports*, 8(1):6687, 2018.

[30] Jean-Charles Arnault, David Eon, Clément Hébert, Davy Carole, Franck Omnes, Etienne Gheeraert, et al. Etching mechanism of diamond by ni nanoparticles for fabrication of nanopores. *Carbon*, 59:448–456, 2013.

[31] Kang Liu, Zhijun Lv, Bing Dai, Guoyang Shu, Jiwen Zhao, Benjian Liu, Weihua Wang, Jingjing Xue, Kaili Yao, Mingqi Sun, et al. High-selectivity anisotropic etching of single-crystal diamond by h plasma using iron catalysis. *Diamond and Related Materials*, 86:186–192, 2018.

[32] W Smirnov, JJ Hees, D Brink, W Müller-Sebert, A Kriele, Oliver Aneurin Williams, and CE Nebel. Anisotropic etching of diamond by molten ni particles. *Applied Physics Letters*, 97(7):073117, 2010.

[33] Tim Schröder, Sara L Mouradian, Jiabao Zheng, Matthew E Trusheim, Michael Walsh, Edward H Chen, Luozhou Li, Igal Bayn, and Dirk Englund. Quantum nanophotonics in diamond. *JOSA B*, 33(4):B65–B83, 2016.

[34] Kenichi Ohno, F Joseph Heremans, Lee C Bassett, Bryan A Myers, David M Toyli, Ania C Bleszynski Jayich, Christopher J Palmstrøm, and David D Awschalom. Engineering shallow spins in diamond with nitrogen delta-doping. *Applied Physics Letters*, 101(8):082413, 2012.

[35] JR Rabeau, Patrick Reichart, Grigori Tamanyan, DN Jamieson, Steven Prawer, Fedor Jelezko, Torsten Gaebel, Iulian Popa, Michael Domhan, and J Wrachtrup. Implantation of labelled single nitrogen vacancy centers in diamond using n 15. *Applied Physics Letters*, 88(2):023113, 2006.

[36] Ariful Haque and Sharaf Sumaiya. An overview on the formation and processing of nitrogen-vacancy photonic centers in diamond by ion implantation. *Journal of Manufacturing and Materials Processing*, 1(1):6, 2017.

[37] J Meijer, B Burchard, M Domhan, C Wittmann, Torsten Gaebel, I Popa, F Jelezko, and J Wrachtrup. Generation of single color centers by focused nitrogen implantation. *Applied Physics Letters*, 87(26):261909, 2005.

[38] Ettore Bernardi, Richard Nelz, Selda Sonusen, and Elke Neu. Nanoscale sensing using point defects in single-crystal diamond: recent progress on nitrogen vacancy center-based sensors. *Crystals*, 7(5):124, 2017.

[39] Marcus W Doherty, Viktor V Struzhkin, David A Simpson, Liam P McGuinness, Yufei Meng, Alastair Stacey, Timothy J Karle, Russell J Hemley, Neil B Manson, Lloyd CL Hollenberg, et al. Electronic properties and metrology of the diamond nv-center under pressure. *arXiv preprint arXiv:1305.2291*, 2013.

[40] Shimon Kolkowitz, Ania C Bleszynski Jayich, Quirin P Unterreithmeier, Steven D Bennett, Peter Rabl, JGE Harris, and Mikhail D Lukin. Coherent sensing of a mechanical resonator with a single-spin qubit. *Science*, 335(6076):1603–1606, 2012.

[41] Preeti Ovartchaiyapong, Kenneth W Lee, Bryan A Myers, and Ania C Bleszynski Jayich. Dynamic strain-mediated coupling of a single diamond spin to a mechanical resonator. *Nature communications*, 5:4429, 2014.

[42] ER MacQuarrie, TA Gosavi, NR Jungwirth, SA Bhave, and GD Fuchs. Mechanical spin control of nitrogen-vacancy centers in diamond. *Physical review letters*, 111(22):227602, 2013.

[43] J Shao, G Liu, and L Zhou. Biomimetic nanocoatings for structural coloration of textiles. In *Active Coatings for Smart Textiles*, pages 269–299. Elsevier, 2016.

[44] University of Cambridge. *Triangles are the strongest shape*, 2016. `https://undergroundmathematics.org/thinking-about-geometry/triangles-are-the-strongest-shape` [Retrieved July 22, 2019].

[45] Brian. *There's nothing particularly "spooky" about avoided crossing*, 2014. `https://gravityandlevity.wordpress.com/2014/04/08/avoided-crossing/` [Retrieved August 12, 2019].

[46] Takatoshi Yamada, Hiromichi Yoshikawa, Hiroshi Uetsuka, Somu Kumaragurubaran, Norio Tokuda, and Shin-ichi Shikata. Cycle of two-step etching process using icp for diamond mems applications. *Diamond and related materials*, 16(4-7):996–999, 2007.

[47] Maximilian Ruf, Mark IJspeert, Suzanne van Dam, Nick de Jong, Hans van den Berg, Guus Evers, and Ronald Hanson. Optically coherent nitrogen-vacancy centers in μm-thin etched diamond membranes. *Nano letters*, 2019.

[48] GF Ding, HP Mao, YL Cai, YH Zhang, X Yao, and XL Zhao. Micromachining of cvd diamond by rie for mems applications. *Diamond and related materials*, 14(9):1543–1548, 2005.

[49] Linh M Pham, Stephen J DeVience, Francesco Casola, Igor Lovchinsky, Alexander O Sushkov, Eric Bersin, Junghyun Lee, Elana Urbach, Paola Cappellaro, Hongkun Park, et al. Nmr technique for determining the depth of shallow nitrogen-vacancy centers in diamond. *Physical Review B*, 93(4):045425, 2016.

[50] L Rondin, G Dantelle, A Slablab, F Grosshans, F Treussart, P Bergonzo, S Perruchas, T Gacoin, M Chaigneau, H-C Chang, et al. Surface-induced charge state conversion of nitrogen-vacancy defects in nanodiamonds. *Physical Review B*, 82(11):115449, 2010.

[51] Donggyu Kim, Mohamed I Ibrahim, Christopher Foy, Matthew E Trusheim, Ruonan Han, and Dirk R Englund. A cmos-integrated quantum sensor based on nitrogen–vacancy centres. *Nature Electronics*, 2(7):284–289, 2019.

[52] Wikipedia. *Laser pointer*, 2019. https://en.wikipedia.org/wiki/Laser_pointer [Retrieved December 9, 2019].

[53] NICHIA. *Green Laser Diode NDG4216*, 1 2013.

[54] OSRAM OS. *PL520*, 11 2018.

[55] Lucio Robledo, Lilian Childress, Hannes Bernien, Bas Hensen, Paul FA Alkemade, and Ronald Hanson. High-fidelity projective read-out of a solid-state spin quantum register. *Nature*, 477(7366):574, 2011.

[56] Samuel J Whiteley, Gary Wolfowicz, Christopher P Anderson, Alexandre Bourassa, He Ma, Meng Ye, Gerwin Koolstra, Kevin J Satzinger, Martin V Holt, F Joseph Heremans, et al. Probing spin-phonon interactions in silicon carbide with gaussian acoustics. *arXiv preprint arXiv:1804.10996*, 2018.

[57] ST Microelectronics. *Silicon Carbide*, 2019. https://www.st.com/content/st_com/en/about/innovation---technology/SiC.html [Retrieved December 9, 2019].